



Contents lists available at ScienceDirect

International Journal of Heat and Mass Transfer

journal homepage: www.elsevier.com/locate/hmt

Numerical investigation of conjugate heat transfer in a pillow-plate heat exchanger

A. Zibart^a, E.Y. Kenig^{a,b,*}^a Chair of Fluid Process Engineering, Paderborn University, Pohlweg 55, Paderborn 33098, Germany^b Gubkin Russian State University of Oil and Gas, Moscow, Russian Federation

ARTICLE INFO

Article history:

Received 8 July 2020

Revised 21 September 2020

Accepted 3 October 2020

Keywords:

Pillow plate

Conjugate heat transfer

CFD

Design methods

ABSTRACT

Pillow Plate Heat Exchangers (PPHX) are composed of several pillow plates arranged parallel to each other, with one flow path inside the plates (inner channel flow) and another in the spaces between adjacent plates (outer channel flow). In research studies published by now, the transport phenomena in these two flow paths have mostly been treated in a separate manner. Such a treatment does not permit to identify important effects, e.g., unfavourable thermal interaction between the inner and outer channel flow caused by predominant recirculation zones, or the influence of the material used for the pillow plate manufacturing. In this work, for the first time, conjugate heat transfer modelling and CFD-based simulations were carried out for a PPHX operated in countercurrent mode. This allowed a detailed analysis of the individual thermal resistances in a PPHX. Based on the results of this analysis, approaches for the correct calculation of these thermal resistances were created.

© 2020 Elsevier Ltd. All rights reserved.

1. Introduction

Pillow plates appeared in the 1990s opened up new possibilities for the design of heat transfer equipment. Their wavy geometry results in beneficial thermohydraulic properties, while high-grade automated manufacturing can be carried out very flexibly and at a low price. For manufacturing of pillow plates, two metal sheets, usually made of stainless steel, are superimposed and welded by computer numerical controlled (cnc) laser in a specific spot pattern. Subsequently, the edges of the sheets are welded and the inlet and outlet nozzles are joined. Through these nozzles, the sheets are pressurized from the inside by an incompressible medium, e.g. water, which deforms the sheets resulting in a pillow-like shell structure, to which they owe their name.

Due to this shell structure, pillow plates are characterized by a high structural strength, so that burst pressures of several hundred bar can be achieved depending on the choice of the welding spot pattern ($2s_L, s_T, d_{SP}$, cf. Fig. 1) and sheet thickness. Furthermore, no supporting structures are required, allowing for lightweight constructions. The fully welded design makes pillow plates hermetically sealed, ensuring a high level of operational reliability. If sheets with significantly different thicknesses are used in the production of a pillow plate, only the thinner sheet is deformed while the thicker sheet remains even, resulting in a so-called "single em-

bossed" pillow plate (cf. Fig. 1). This design is mainly used for the production of vessels (e.g. reactors, fermenters, dryers). After the welding process, yet before the inflation process, the sheets are bent into a cylindrical shape by means of rolling and finally welded to form the vessel jacket. After the bottom and top elements of the vessel have been joined, the inflation process takes place, in which the outer surface of the vessel is given the pillow-like structure, but the inside remains flat and is therefore easy to clean and less susceptible to fouling. The thermal management of the vessel content is then achieved by guiding a fluid through the inner channel of the vessel pillow plate jacket. Compared to conventional half-pipe coil jacket vessels, much larger heat transfer surface can be realised with a pillow plate jacket vessel design, while manufacturing is much cheaper and easier. Choosing the same thickness of the two superimposed sheets during the production of pillow plates causes the sheets to deform uniformly during the inflation process and form a symmetrical pillow structure which is referred to as "double embossed" (cf. Fig. 1). This type of pillow plate is mainly used for the design of pillow plate heat exchangers (PPHX, cf. Fig. 1).

Several pillow plates are arranged parallel with a certain distance from each other to a package and inserted into a housing. In addition to a flow path IC (inner channel), created by the inner channels of the pillow plates, a further flow path OC (outer channel) is formed by the channels, which result from the space between adjacent pillow plates. The sheet material separates the media in IC and OC and thus enables indirect heat transfer. By

* Corresponding author.

E-mail address: eugen.y.kenig@upb.de (E.Y. Kenig).

Nomenclature

A	area, [m^2]
c_p	specific heat capacity, [J/kgK]
d	diameter, [m]
f_{FIT}	fit function, [-]
h	heat transfer coefficient, [$\text{W}/\text{m}^2\text{K}$]
\hat{h}	heat transfer coefficient (constant temperature boundary condition), [$\text{W}/\text{m}^2\text{K}$]
L	length, [m]
\dot{m}	mass flow rate, [kg/s]
Nu	Nusselt number, [-]
Pr	Prandtl number, [-]
\dot{Q}	heat flow rate, [W]
\dot{q}	heat flux, [W/m^2]
\dot{q}^*	reference boundary heat flux, [W/m^2]
R_{th}	thermal resistance, [K/W]
r_{th}	specific thermal resistance, [Km^2/W]
Re	Reynolds number, [-]
s	welding spot pitch, [m]
T	thermodynamic temperature, [K]
u	velocity, [m/s]
V	volume, [m^3]
x, y, z	Cartesian coordinates, [m]
y^+	dimensionless wall distance, [-]

Greek symbols

Δp	pressure drop, [Pa]
δ	distance/thickness, [m]
$\zeta_{\Delta p}$	Darcy friction factor, [-]
η	fin efficiency, [-]
ϑ	temperature, [$^\circ\text{C}$]
λ	thermal conductivity, [W/mK]
μ	dynamic viscosity, [Pa s]
ν	kinematic viscosity, [m^2/s]
ρ	density, [kg/m^3]
ψ	ratio of surface areas, [-]

Subscripts

$CALC$	values calculated by approaches introduced in this paper
cs	cross-section
F	fluid
fin	fin
FIT	values corrected by a fit function
h	hydraulic
IC	inner channel
in	inflow
L	longitudinal
m	mean value
max	maximum value
OC	outer channel
P	plate
Ref	reference value
SD	simulation domain
SIM	simulation result
SP	welding spot
T	transversal
tot	total
w	wall

varying the distance of the pillow plates from each other, the cross-sectional area of the OC can be adjusted, generally allowing a lower pressure drop compared to the IC. The OC is usually not fully welded, so that in contrast to IC, the channels are

cleanable. This makes PPHX also suitable for dirty and highly viscous media if they are fed into the OC. Moreover, PPHX combine the advantages of the most commonly used conventional heat exchanger types. They are as pressure and temperature resistant as shell-and-tube heat exchangers, and enable cost-efficient manufacturing and compact design, which is characteristic for plate heat exchangers. PPHX are commonly used as top condensers in distillation columns and as falling film evaporators in food industry as well as in pulp and paper industry. In spite of the advantages of pillow plate based equipment, their market penetration is currently still slow. This mainly results from the fact that, compared to conventional apparatuses, comprehensive design principles do not yet exist and therefore there are still considerable uncertainties in the dimensioning of such apparatuses. Until about a decade ago, pillow plates were totally unexplored, but in the recent past this has changed mainly due to research activities at Paderborn University.

In 2007, Mitrovic and Peterson [1] published first experimental results regarding the single-phase flow in pillow plate channels, where forced convection heat transfer and pressure drop for inner channel flow were investigated with a single, electrically heated pillow plate. Furthermore, they showed results on the condensation in the outer channel of a PPHX, where the phase change of isopropanol vapour was caused by means of cooling with water in the inner channel. This was followed by numerical investigations of Mitrovic and Maletić [2] focusing on inner channel flow and heat transfer. The complex, three-dimensional geometry of the pillow plates was approximated by trigonometric functions and the flow was assumed to be laminar for the CFD simulations, although Reynolds numbers of up to 3800 were investigated. As thermal boundary condition at the channel wall they specified a constant wall temperature. In contrast to [1], the investigations were not limited to just one pillow plate geometry, but a variation of the welding spot pattern as well as the inflation height was performed.

Piper et al. [3,4] were the first to succeed in accurately reconstructing the complex pillow plate geometry. They used finite element analysis to numerically reproduce the inflation process of pillow plates. A comparison with measurements obtained by means of contour gauge for an existing pillow plate resulted in a maximum deviation regarding the numerically determined displacements of less than 4%. Based on an extensive study, with varying geometry parameters of the welding spot pattern and the pillow plate inflation height as well as the distance between the neighbouring plates, they developed correlations for design-relevant parameters like heat transfer surface area and channel volume for the inner and outer channels. Afterwards, these parameters were used for the calculation of the hydraulic diameter and the mean channel cross-section.

In the next step, a comprehensive CFD study to gain a deeper understanding of the transport phenomena present in the inner channel for $1000 \leq Re_{IC} \leq 8000$ and $5 \leq Pr \leq 100$ was carried out in [5]. In contrast to [2], turbulence was considered and described statistically by applying the Reynolds-Averaged-Navier-Stokes (RANS) equations and calculating the Reynolds stresses by means of the realizable $k - \epsilon$ turbulence model [6]. A validation with measurements revealed that pressure drop and heat transfer for single-phase IC flow can be predicted with a maximum deviation of 8% and 15%, respectively [7,8].

Based on the resulting IC flow patterns, the pillow plates were sub-classified into "longitudinal type", "mixed type" and "transversal type" depending on the welding spot parameters. Characteristic for a "longitudinal type" pillow plate is that the recirculation zones formed behind the welding spots have a flame-like shape, whereas for a "transversal type" pillow plate, the recirculation zones extend to the next downstream welding spot. For both pillow plate types, the resulting flow pattern is largely independent of the Reynolds

number. In the case of "mixed type" pillow plates, on the other hand, the flow pattern for $Re_{IC} \leq 2000$ is similar to that of a "longitudinal type" pillow plate and transforms with increasing Reynolds number to that of a "transversal type".

Later Piper et al. [9] have extended their numerical investigations of IC flow to a wider range of geometrical parameters, whereby only "longitudinal type" and "transversal type" pillow plates were investigated, since "mixed type" pillow plates reveal low application potential. Based on the results obtained and taking into account the outcomes of [5], they derived correlations for Darcy friction factor (ζ_{DP}) and Nusselt number in form of a power law approach, allowing the calculation of pressure loss and heat transfer with an accuracy of $\pm 6\%$ and $\pm 15\%$, respectively, for a wide range of applicability in terms of geometrical parameters, flow conditions ($1000 \leq Re_{IC} \leq 8000$) and fluid properties ($1 \leq Pr \leq 150$).

Furthermore, a modelling approach based on the flow pattern was developed for heat transfer. Here, the flow in IC of the pillow plates was broken down into two zones, the recirculation zones and the meandering core flow, which were then modelled separately. Again, the deviation of the modelling approach compared to the CFD simulations was $\pm 15\%$. In [10,11] Piper et al. also carried out numerical investigations of OC flow. In [10], turbulence was considered in the performed CFD simulations utilizing the realizable $k - \varepsilon$ turbulence model, as it was done for inner channel flow. This resulted in a strong underestimation of the pressure drop compared to experiments, with a deviation of 19%. Therefore, in [11], the more advanced elliptic blending $k - \varepsilon$ model [12] was used instead, which is able to consider anisotropy in turbulence and is more accurate in predicting flow separation and reattachment. This reduced the deviations from the experimental results to 5%.

An efficiency analysis was carried out for IC and OC by comparing the thermohydraulic efficiency of pillow plate flow channels with pipes, defining the thermohydraulic efficiency as the ratio of heat transfer rate to pumping power. This comparison showed that the operation of PPHX can be judged reasonable for Reynolds numbers of less than 3000 in IC and less than 10000 in OC.

In most of the papers published up to now, both IC and OC flow and heat transfer in PPHX have been considered separately. For CFD simulations, simplified boundary conditions, such as a constant wall temperature, were applied, whereas in experiments, a single, electrically heated pillow plate was used, resulting in an approximately constant wall heat flux. These simplifications do not correspond to reality and therefore, the influence of the wall material as well as unfavourable thermal interactions between IC and OC flow caused by the existing recirculation zones in the channels cannot be taken into account. Especially in case of OC flow, a non-negligible error in the heat transfer prediction is to be expected, since, compared to IC flow, the thermally active heat transfer surface is increased by the welding spot surfaces, which can be inter-

preted as fins. It is known from the literature that the thermal activity of fins expressed by the fin efficiency depends on heat transfer coefficients, geometric parameters and thermal conductivity of the solid material. Imposing a constant wall temperature leads to the situation that temperature gradients in the welding spots vanish. This means that the fins are considered to be thermally fully active having a fin efficiency equal to one, which can only be approximately applied to sheet materials with very high thermal conductivity. However, the most commonly used material for pillow plates is stainless steel having a relatively low thermal conductivity. For this reason, in this work, so-called conjugate heat transfer (CHT) modelling was applied and corresponding CFD simulations were performed focusing on the fully developed flow section of a countercurrently operated PPHX. In this case, IC and OC flow are simulated simultaneously under consideration of the thermal coupling through the sheet material. In addition to a variation of the flow velocities, the influence of sheet material and thickness on the overall heat transfer was also investigated by examining pillow plates made of stainless steel and of aluminium, with thicknesses of 1 mm and 2 mm.

2. Geometrical aspects

The investigations carried out in this work are limited to a PPHX configuration in which the pillow plates are arranged parallel to each other at a distance of $\delta_{OC} = 13$ mm. A specific pillow plate geometry in double embossed design was chosen, with an inflation height of $\delta_{IC} = 7$ mm and a typical triangular welding spot pattern ($\arctan(2s_L/s_T) \approx 60^\circ$) having the dimensions $2s_L = 72$ mm, $s_T = 42$ mm and a welding spot diameter of $d_{SP} = 12$ mm (cf. Fig. 1). The choice was made for this PPHX configuration, since the results of numerical and experimental studies have already been published for both IC and OC, thus providing a good basis for validation. In order to evaluate the effect of the plate thickness on heat transfer, the plate thickness was varied, with $\delta_P \in \{1 \text{ mm}, 2 \text{ mm}\}$. Whereas $\delta_P = 1 \text{ mm}$ is very common for pillow plates, $\delta_P = 2 \text{ mm}$ represents the practical maximum value for the plate thickness and is usually met in high-pressure applications only.

The pillow plate geometry was generated by a forming simulation based on the FEM methods imitating the inflation process. This simulation was carried out in analogy to the work of Piper et al. [4] using the software ABAQUS 2017 (Dassault Systèmes). For reduction of the computational effort, only a characteristic section of the pillow plate with the projection area $A_0 = (0.5s_T) \cdot s_L$ was examined, taking advantage of all geometrical symmetries and thus also focusing only on one of the two pillow plate forming metal sheets. Furthermore, shell theory was applied, allowing a dimensional reduction of the metal sheet to its middle surface. For this reference surface, the mechanical equations were solved discretely using the Mindlin-Reissner plate theory, which models

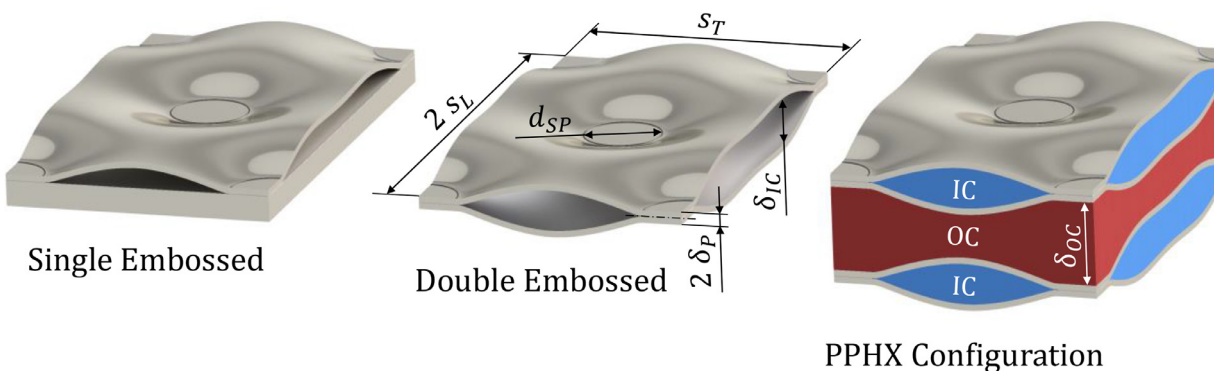


Fig. 1. Periodic sections of a single embossed pillow plate (left), a double embossed pillow plate (middle) and a PPHX composed of double embossed pillow plates (right).

the resulting strains and stresses in the thickness direction of the sheet by kinematic approaches. The result of this forming simulation represents the three-dimensionally deformed middle surface of the sheet. Using the CAD tool Inventor 2018 by Autodesk, the deformed middle surface was then converted to a volume body by adding the thickness dimension, resulting in a 3D model of the sheet. Furthermore, the deformed middle surface of the sheet was used to create 3D models of the inner fluid volumes of IC and OC. The generated 3D models of the metal sheet as well as the IC and OC fluid volumes were then used to define the computational domains for the CFD simulations carried out within the scope of this work. The hydraulic diameters of IC and OC channels were calculated according to Eqs. (1) and (2) by means of the channel volume and the wetted surface area, as defined by Piper et al. [4]:

$$\bar{d}_{h,IC} = \frac{4 \cdot V_{IC}}{A_{w,IC}} \quad (1)$$

$$\bar{d}_{h,OC} = \frac{4 \cdot V_{OC}}{A_{w,OC}} \quad (2)$$

Thus, for the PPHX configuration considered in this work, hydraulic diameters of $\bar{d}_{h,IC} = 9.373$ mm and $\bar{d}_{h,OC} = 16.993$ mm were obtained.

It should be mentioned that, compared to IC, the wall surface area of OC is enlarged by the welding spot surface A_{SP} . For the pillow plate considered in this paper, this surface area enlargement can be quantified by means of the parameter introduced in Eq. (3)

$$\psi_{SP} = \frac{A_{SP}}{A_{w,IC}} = \frac{A_{w,OC} - A_{w,IC}}{A_{w,IC}} \quad (3)$$

with $\psi_{SP} \approx 0.081$. Thus, the heat transfer surface area for the OC flow is 8.1% larger than for the IC flow. For the calculation of the mean flow velocities in the PPHX channels, again approaches by Piper et al. [4] were used. Thus, the mean cross-sections of IC and OC are given as channel volume related to the main flow length. In the CFD simulations performed, the main flow length corresponds to the length of the simulation domain (L_{SD}). Consequently, the cross-sections of the simulation domains used were calculated by Eqs. (4) and (5):

$$\bar{A}_{cs,IC} = \frac{V_{IC}}{L_{SD}} \quad (4)$$

$$\bar{A}_{cs,OC} = \frac{V_{OC}}{L_{SD}} \quad (5)$$

3. Process parameters

In order to analyse the influence of the operating condition of the PPHX on heat transfer, the flow velocities in IC ($u_{m,IC}$) and OC ($u_{m,OC}$) were varied in the numerical investigations carried out in this study. Since the efficiency analysis performed in [11] revealed that the operation of a PPHX is most reasonable for Reynolds numbers $Re_{OC} < 10000$ in OC and for $Re_{IC} < 3000$ in IC, the operating conditions were restricted to $Re_{OC} = 5000, 7500, 10000$ and $Re_{IC} = 1000, 2000, 3000$ (cf. Table 1). The Reynolds numbers are defined as follows:

$$Re_{OC} = \frac{u_{m,OC} \cdot \bar{d}_{h,OC}}{\nu} \quad (6)$$

$$Re_{IC} = \frac{u_{m,IC} \cdot \bar{d}_{h,IC}}{\nu} \quad (7)$$

Re_{IC} was initially kept constant at $Re_{IC} = 2000$, while Re_{OC} was changed according to the value set shown above. In the next step, simulations were performed with Re_{OC} kept constant at

Table 1

Summary of the investigated operating conditions.

Re_{IC}	Re_{OC}		
	5000	7500	10000
1000	-	-	C4
2000	C1	C2	C3
3000	-	-	C5

Table 2

Fluid properties used in the simulation study.

Medium	ρ	μ	c_p	λ_F	Pr
- Water	kg/m ³ 997.561	Pas 8.8871E-4	J/kgK 4181.72	W/mK 0.620271	- 5.99

$Re_{OC} = 10000$, while the Reynolds number in IC was reduced to $Re_{IC} = 1000$ or increased to $Re_{IC} = 3000$. A total of five different flow configurations were investigated, which are summarised in Table 1 and denoted by the corresponding case numbers (C1-C5).

Water was chosen as the process medium in both IC and OC of the PPHX. The fluid properties, which are shown in Table 2, were assumed to be identical in both flow channels and temperature-independent.

The target mass flow rates have to be adjusted in the simulations in order to match the Reynolds numbers from the corresponding simulated cases (C1-C5, cf. Table 1). The flow rates were calculated by Eqs. (8) and (9), obtained using Eqs. (6) and (7).

$$\dot{m}_{OC} = \rho \cdot \bar{A}_{cs,OC} \cdot u_{m,OC} = \frac{\rho \cdot \bar{A}_{cs,OC} \cdot v \cdot Re_{OC}}{\bar{d}_{h,OC}} \quad (8)$$

$$\dot{m}_{IC} = \rho \cdot \bar{A}_{cs,IC} \cdot u_{m,IC} = \frac{\rho \cdot \bar{A}_{cs,IC} \cdot v \cdot Re_{IC}}{\bar{d}_{h,IC}} \quad (9)$$

In addition to the influence of the flow configuration on heat transfer, the influence of the sheet material was also investigated. The most common material used to manufacture pillow plates is stainless steel, with varying alloys to adjust it to requirements, while the thermal conductivity of stainless steel is nearly independent of the alloy composition. The thermal conductivity used within this work was $\lambda_P = 15$ W/mK. A promising alternative to stainless steel is aluminium, which has a significantly higher thermal conductivity than stainless steel and would therefore have a positive effect on heat transfer in PPHX. Furthermore, the density of aluminium is more than 60% lower compared to stainless steel, making a lighter apparatus design achievable. The drawback of the lower mechanical strength of aluminium could be compensated by adjusting the sheet thickness, while the advantages could still prevail due to the much lower density and much higher thermal conductivity compared to stainless steel. For this reason, aluminium was considered as an additional sheet material to study. In contrast to stainless steel, the thermal conductivity of aluminium can vary significantly depending on the alloy and has the value of $\lambda_P \approx 160$ W/mK for technically relevant alloys, while pure aluminium has a thermal conductivity of $\lambda_P = 237$ W/mK. To identify the maximum potential of pillow plates made out of aluminium, the simulations were performed assuming pure aluminium. Since only steady-state simulations were carried out in this work, the only relevant material property of the sheet material is the thermal conductivity. Therefore, further material properties will not be discussed.

4. Heat transfer characteristics

The driving force for heat transfer in a PPHX is the temperature difference between OC and IC flow, while the total thermal resistance between them determines the magnitude of the induced heat flow. Formed by a serial combination of the three partial thermal resistances $R_{th,OC}$, $R_{th,P}$, $R_{th,IC}$, the total thermal resistance can be calculated as follows:

$$R_{th,tot} = R_{th,OC} + R_{th,P} + R_{th,IC} = \frac{T_{m,OC} - T_{m,IC}}{\dot{Q}} \quad (10)$$

While $R_{th,OC}$ and $R_{th,IC}$ characterize the convective heat transfer between IC respectively OC flow and the corresponding pillow plate surface, $R_{th,P}$ determines the heat transfer inside the metal sheets based on pure thermal conduction. From the results of the CHT simulations performed in this study, $R_{th,tot}$ was calculated for a specified evaluation section (explained in Section 6) as the ratio of driving temperature difference between mean bulk temperatures of OC and IC and the heat flow rate (Eq. (10)). The required mean bulk temperatures were calculated as adiabatic mixing temperatures of the fluid flows, with integration performed for the respective flow (IC/OC) over the inlet ($A_{CS,i,1}$) and outlet cross-section ($A_{CS,i,2}$) of the evaluation section:

$$T_{m,i} = \frac{\int_{A_{CS,i,1}} uT \, dA + \int_{A_{CS,i,2}} uT \, dA}{2 \cdot \int_{A_{CS,i,1}} u \, dA} \quad \text{with } i \in \{IC, OC\}$$

and $\int_{A_{CS,i,1}} u \, dA = \int_{A_{CS,i,2}} u \, dA$

$$(11)$$

The heat flow rate transferred in the evaluation section, was calculated as surface integral of the boundary heat flux over the interface between fluid flow and metal sheet as follows:

$$\dot{Q} = \int_{A_w} \dot{q} \, dA \quad (12)$$

The thermal resistances in Eq. (10) behave inversely proportional to the total available heat transfer surface, since for constant temperature difference and constant mean heat transfer coefficients, the transferred heat flow rate increases with increasing surface area. Thus, the thermal resistances mentioned above are extensive quantities making a direct comparison of different PPHX designs difficult. For this reason, a normalisation of the thermal resistances was introduced, where the wetted surface area of IC ($A_{w,IC}$) was chosen as reference. Hence, the specific thermal resistances are defined as the ratio of the driving temperature difference to the reference boundary heat flux \dot{q}^* :

$$r_{th,i} = R_{th,i} \cdot A_{w,IC} = \frac{\Delta T}{\dot{Q}/A_{w,IC}} = \frac{\Delta T}{\dot{q}^*}, \quad \text{with } \dot{q}^* = \frac{\dot{Q}}{A_{w,IC}} \quad (13)$$

In the following sections, the individual partial resistances, of which $R_{th,tot}$ respectively $r_{th,tot}$ are composed, are explained in more detail.

4.1. Outer channel

Applying the Newtonian law, \dot{q}^* can be expressed for OC flow via the mean heat transfer coefficient $h_{m,OC}$, heat transfer surface ($A_{w,IC} + A_{SP}$) and driving temperature difference ($T_{m,OC} - T_{w,OC}$) according to the following equation:

$$\dot{q}^* = \frac{\dot{Q}}{A_{w,IC}} = \frac{h_{m,OC}(A_{w,IC} + A_{SP})(T_{m,OC} - T_{w,OC})}{A_{w,IC}} \quad (14)$$

In the simulations performed, the mean wall temperature $T_{w,OC}$ was determined as the surface average temperature of the interface between the fluid and the metal sheet by the following, generally valid approach:

$$T_{w,i} = \frac{\int_{A_{w,i}} T \, dA}{\int_{A_{w,i}} dA} \quad (15)$$

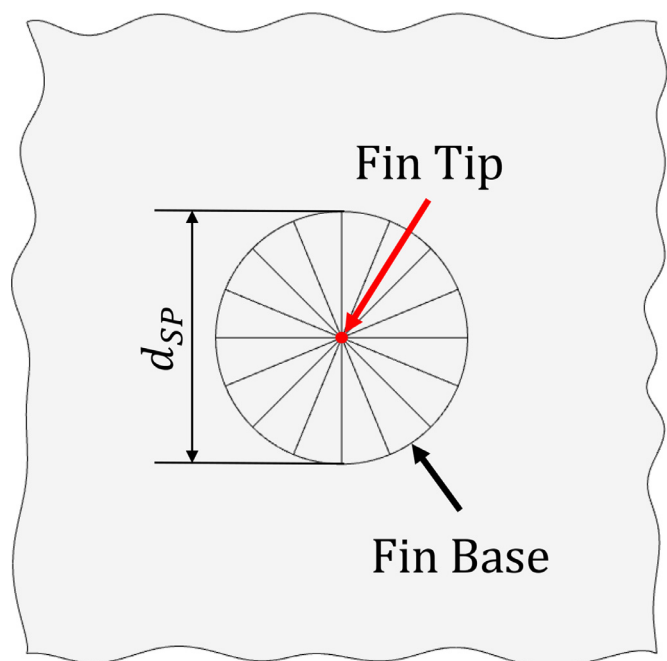


Fig. 2. Cut-out view around a welding spot and illustration of the idea that welding spots are composed of several triangular fins.

The thermal resistances $r_{th,OC,SIM}$ obtained from the simulations were calculated according to Eq. (13), but an equivalent expression can be derived by means of $h_{m,OC}$ and ψ_{SP} , as given by Eq. (16):

$$r_{th,OC,SIM} = \frac{T_{m,OC} - T_{w,OC}}{\dot{q}^*} = \frac{A_{w,IC}}{h_{m,OC}(A_{w,IC} + A_{SP})} = \frac{1}{h_{m,OC}(1 + \psi_{SP})} \quad (16)$$

In fact, the thermal resistance of the OC flow can be interpreted as a parallel combination of two thermal resistances. On the one hand, thermal resistance results from the convective heat transfer via the partial heat transfer surface area $A_{w,IC}$. On the other hand, heat, which is exchanged between the fluid and the welding spot surfaces, must be transported inside the metal sheet through in-plane heat conduction causing an additional thermal resistance. This results in the formation of temperature gradients within the metal sheet in radial direction of the welding spots, which leads to a reduction of the effective temperature difference between the welding spot surfaces and the fluid. Hence, the welding spot surfaces are not fully thermally active. Assuming a constant heat flux density on the outer pillow plate surface, the temperature gradient must vanish for reasons of symmetry in the surface-normal centreline of the welding spots, so that a temperature extremum is to be expected here. Based on these considerations, the welding spots can be estimated as a composition of several triangular fins. These fins have a fin height of $L_{fin} = 0.5 \cdot d_{SP}$ and a thickness of $\delta_{fin} = 2\delta_P$ (two metal sheets are superimposed at the welding spots) and are touching each other with their fin tip in the centre-line of the welding spots (cf. Fig. 2).

The thermal activity of a fin depends on the heat transfer coefficient, the thermal conductivity of the fin material as well as the thickness and height of the fin. Calculation methods can be found for example in [13]. When applied to the welding spot surfaces, the fin efficiency is calculated as follows:

$$\eta_{SP} = \tanh \left(\sqrt{\left(\frac{2h_{m,OC}}{\lambda_P \delta_{fin}} \right)} L_{fin} \right) / \left(\sqrt{\left(\frac{2h_{m,OC}}{\lambda_P \delta_{fin}} \right)} L_{fin} \right) \quad (17)$$

The determination of heat transfer coefficients for OC by means of CHT simulations is, however, very costly, and the results depend

not only on the flow conditions in OC, but also on the thickness and material of the metal sheet. By contrast, the determination of heat transfer coefficients for OC assuming a constant wall temperature is much simpler, since it is sufficient to perform simulations for a single periodic section of OC, as was done in [11]. However, the assumption of a constant wall temperature means that the temperature gradients arising in the welding spots are not taken into account. Thus, the welding spot surfaces are always acting fully thermally active, which corresponds to a fin efficiency of $\eta_{SP} = 1$ and would only apply to an infinitely high thermal conductivity of the metal sheet. Nevertheless, with the fin efficiency according to Eq. (17), \dot{q}^* can be calculated approximately for OC by using the heat transfer coefficient $\hat{h}_{m,OC}$, which is valid for constant wall temperature:

$$\dot{q}^* \approx \frac{\hat{h}_{m,OC}(A_{w,IC} + \eta_{SP}A_{SP})(T_{m,OC} - T_{w,OC})}{A_{w,IC}} \quad (18)$$

This results in the following simplified approach to determine the thermal resistance for OC based on $\hat{h}_{m,OC}$ and η_{SP} , with the latter obtained by using $\hat{h}_{m,OC}$ instead of $h_{m,OC}$ in Eq. (17):

$$\begin{aligned} r_{th,OC,CALC} &= \frac{A_{w,IC}}{\hat{h}_{m,OC} \cdot A_{w,IC} + \hat{h}_{m,OC} \cdot \eta_{SP} \cdot A_{SP}} \\ &= \frac{1}{\hat{h}_{m,OC}(1 + \eta_{SP}\psi_{SP})} \end{aligned} \quad (19)$$

The deviation between $\hat{h}_{m,OC}$ and $h_{m,OC}$ vanishes in case of thermally fully active welding spots, so that Eq. (19) reduces to Eq. (16) for $\eta_{SP} = 1$. On the other hand, it becomes clear from Eq. (19) that the assumption of thermally fully active welding spots ($\eta_{SP} = 1$) for sheet materials with poor thermal conductivity ($\eta_{SP} \approx 0$) would result in an underestimation of $r_{th,OC}$ with a relative deviation of $\psi_{SP}/(1 + \psi_{SP})$. In case of the investigated pillow plate, this corresponds to an error of about 7.5%, which is non-negligible. The validity of the suggested approach for the calculation of $r_{th,OC}$ is confirmed in Section 7. The value of $\hat{h}_{m,OC}$ required to determine $r_{th,OC}$ could be obtained from a correlation for Nu_{OC} , which is valid for a constant wall temperature:

$$Nu_{OC} = \frac{\hat{h}_{m,OC} \cdot \bar{d}_{h,OC}}{\lambda_F} = f(Re, Pr, Geometry) \quad (20)$$

To derive such a correlation for Nu_{OC} , a comprehensive study should be carried out in future work, in which simplified simulations are performed for OC flow with constant wall temperature boundary condition.

4.2. Solid plate

The specific thermal resistance of the metal sheet is calculated as the difference between the surface average temperatures of the outer and inner pillow plate surface in relation to the reference heat flux:

$$r_{th,P,SIM} = \frac{T_{w,OC} - T_{w,IC}}{\dot{q}^*} \quad (21)$$

The heat transfer in the metal sheet is based on pure heat conduction. If simplified one-dimensional heat conduction is considered, the specific thermal resistance of the sheet could be calculated as follows:

$$r_{th,P,CALC} = \frac{\delta_P}{\lambda_P} \quad (22)$$

In Section 7, we will examine to what extent $r_{th,P,SIM}$ deviates from the simplified calculated $r_{th,P,CALC}$, and a correction function $f_{FIT,P}$ will be introduced to take the three-dimensional effects into account. The value of $r_{th,P,CALC}$ will be adjusted using $f_{FIT,P}$ as follows:

$$r_{th,P,FIT} = r_{th,P,CALC} \cdot f_{FIT,P} \quad (23)$$

4.3. Inner channel

The definition of the specific thermal resistance for IC is similar to that of $r_{th,OC}$, but surface area enlargement due to the welding spots (ψ_{SP}) is omitted in the denominator, since the effective heat transfer surface area equals the reference area $A_{w,IC}$:

$$\begin{aligned} r_{th,IC,SIM} &= \frac{T_{w,IC} - T_{m,IC}}{\dot{q}^*} = \frac{A_{w,IC}(T_{w,IC} - T_{m,IC})}{\dot{Q}} \\ &= \frac{A_{w,IC}(T_{w,IC} - T_{m,IC})}{h_{m,IC}A_{w,IC}(T_{w,IC} - T_{m,IC})} = \frac{1}{h_{m,IC}} \end{aligned} \quad (24)$$

In [9], based on a comprehensive simulation study, correlations were derived for Nusselt number in IC with a wide range of validity. However, the simulations were performed for a small periodic element of IC with the specification of a constant wall temperature, so that the thermal boundary condition used hardly corresponds to reality. Using these correlations, the heat transfer coefficient $\hat{h}_{m,IC}$, which is valid for a constant wall temperature, could be determined using the following definition of the Nusselt number for IC:

$$Nu_{IC} = \frac{\hat{h}_{m,IC} \cdot \bar{d}_{h,IC}}{\lambda_F} = f(Re, Pr, Geometry) \quad (25)$$

In Section 7, the resulting deviations between $r_{th,IC,SIM}$ and $r_{th,IC,CALC}$, which is calculated according to Eq. (26) using $\hat{h}_{m,IC}$ instead of $h_{m,IC}$, are analysed:

$$r_{th,IC,CALC} = \frac{1}{\hat{h}_{m,IC}} \quad (26)$$

Furthermore, a correction function $f_{FIT,IC}$ will be suggested in Section 7, with which $r_{th,IC,CALC}$ can be adapted to take conjugate heat transfer effects into account:

$$r_{th,IC,FIT} = r_{th,IC,CALC} \cdot f_{FIT,IC} \quad (27)$$

5. CFD simulations

The simulation study carried out in this work comprised two stages. In the first stage, uncoupled simulations of flow in IC and OC were performed. In analogy to [5,10,11], each simulation was limited to a reduced periodic channel section, and a constant temperature was always specified as a thermal boundary condition at the channel walls. On one hand, these simulations were aimed at validation, by comparison with the results obtained by Piper et al. [9–11]. On the other hand, precise values for $\hat{h}_{m,OC}$ and $\hat{h}_{m,IC}$ could be determined from these simulations, which were needed to verify the approach suggested in Section 4.1 and to develop the correction function $f_{FIT,IC}$ mentioned in Section 4.3. In the second stage, CHT simulations were carried out, in which heat transport between OC flow, metal sheet and IC flow was resolved in a coupled manner in order to achieve a realistic reproduction of predominant heat transport processes in a PPHX. Hydraulically and thermally fully developed flow covers major part of the channels in an industrial apparatus. Therefore, this was the focus of the investigations performed. The underlying modelling of the performed CFD simulations is highlighted in the following sections.

5.1. Basic CFD modelling

All simulations were carried out with the software Star-CCM+ 13.02 by Siemens PLM, which is based on the finite volume method. In all cases, it was assumed that the flow is steady-state, single-phase, incompressible and turbulent, having constant fluid properties (Table 2). The turbulence was accounted for statistically, by applying the Reynolds-Averaged-Navier-Stokes (RANS) equations. As described in [5], the Reynolds stresses in

case of IC flow were determined using the realizable $k - \varepsilon$ model [6], which is a two-equation linear eddy viscosity model. For OC flow, instead of the standard elliptic blending $k - \varepsilon$ model [12] used in [11], the lag elliptic blending $k - \varepsilon$ model [14] was used, both being three-equation models. The formulations of the transport equations of the lag elliptic blending $k - \varepsilon$ model and the standard elliptic blending $k - \varepsilon$ model are similar. However, by deriving the lag formulation from a full Reynolds Stress Model (RSM), it is possible to take into account misalignment of stress and strain tensor, so that the turbulent kinetic energy in affected regions is predicted more accurate.

Due to the elliptic blending, both models can also be used in the viscosity dominated area of the turbulent boundary layer, so that no additional wall treatment is necessary. Furthermore, both models are able to capture anisotropy in turbulence. However, in the simulations performed, the lag elliptic blending $k - \varepsilon$ model was numerically more stable than the standard elliptic blending $k - \varepsilon$ model, so that, in contrast to [11], steady-state solutions could always be obtained. Consequently, this resulted in a significant reduction of the computational effort. In all cases, the boundary layers were resolved by the computational mesh down to the viscous sublayer, as boundary layer separations with resulting backflow were to be expected. For this reason, a two-layer formulation was used for the realizable $k - \varepsilon$ model to capture the damping of turbulence near walls. In this context, a reduction to Wolfshtein's one-equation model [15] was used for the viscosity affected region, by solving only the transport equation for k , while ε is determined algebraically. In the fully turbulent region, however, the ordinary formulation of the realizable $k - \varepsilon$ model is retained. The major advantage of the two-layer formulation compared to low Reynolds models is that the steep gradients of ε near walls have no negative effect on the numerical stability.

5.2. Meshing

The mesh generation was performed with the software ICEM by Ansys, because it allows a more detailed generation of block structured meshes than the mesh generator of Star-CCM+. Unstructured meshes were avoided, because they often result in strongly dis-

torted cells or large volume changes between adjacent cells, which in turn leads to numerical inaccuracies. For this reason, a significantly larger number of cells is usually required in comparison to block-structured grids to achieve the same accuracy. The applied cell geometry is hexahedral. For the uncoupled simulations of IC and OC flow as well as for the CHT simulations, the same local discretization was chosen for the corresponding computational domain. Furthermore, the meshes were designed in such a way that in case of the CHT simulations, the cells of the IC and OC domain are congruent with the cells of the plate domain at the corresponding interface (cf. Fig. 3). This was intended to avoid interpolation errors with regard to the calculation of the domain-crossing heat transport. In order to resolve the steep gradients present in the vicinity of the walls and along the edge of the welding spot, a mesh refinement was undertaken in the direction normal to the wall and in the radial direction of the welding spots (cf. Fig. 3).

As explained in the previous section, care has been taken to ensure that the cells closest to the wall are located well within the viscous sublayer. For the final meshes, which are the result of a grid independence study, a maximum dimensionless wall distance of $y^+ = 0.4$ is obtained for OC flow ($Re_{OC} = 10000$), whereas it is $y^+ = 0.2$ for IC flow ($Re_{IC} = 3000$). The total number of computational cells for the CHT simulations is approximately 276 Mio. in case of a 1 mm thick metal sheet, while the total number of cells for a 2 mm thick metal sheet is approximately 316 Mio. Of these, approximately 167 Mio. cells belong to the OC domain, approximately 69 Mio. cells to the IC domain and 40 Mio., respectively 80 Mio., cells to the domain of the metal sheet. The performed grid independence study revealed that a further doubling of the number of cells caused a difference in pressure drop of only 0.03% for IC flow and 0.005% for OC flow, so that the results can be considered as grid independent. For heat transport, a further doubling of the number of grid cells resulted in a deviation of the resulting heat flow rate of about 0.1% only.

5.3. Boundary conditions for the uncoupled simulations

Compared to the forming simulations, in which the simulation domain was reduced to a characteristic section of the pil-

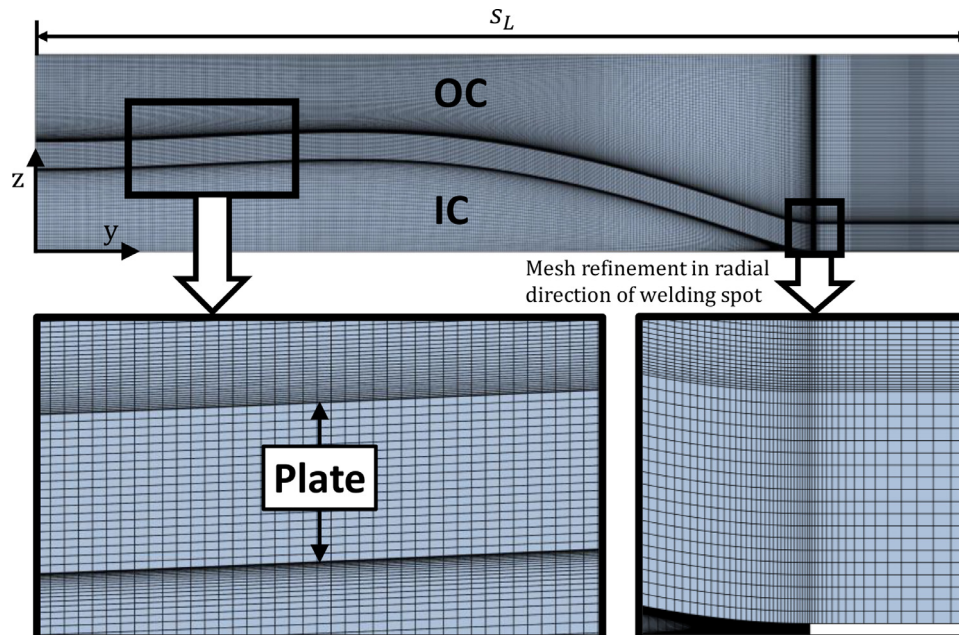


Fig. 3. Representation of the computational mesh used on the basis of a characteristic section with the length s_L .

low plate with a projection area of $A_0 = (0.5s_T) \cdot s_L$, in case of the uncoupled CFD simulations for IC and OC flow, the size of the investigated section was doubled in primary flow direction (y -direction, cf. Fig. 4). This results in geometrical periodicity in the primary flow direction, which allows usage of periodic boundary conditions. After each iteration step, the fields of velocity and turbulence quantities (turbulent kinetic energy, turbulent dissipation rate, reduced stress function) are copied from the downstream boundary of the computational domain to the upstream boundary, thus enabling the investigation of the hydrodynamically fully developed flow based on a strongly reduced computational domain. In the simulations, the pressure drop Δp arising between the periodic boundaries is recalculated iteratively, so that the target mass flow rate predefined according to Eqs. (8) or (9) is achieved. The temperature field is scaled from the downstream to the upstream periodic boundary in such a way that identical heat transfer coefficients are obtained at both boundaries and hence the condition of a thermally fully developed flow is fulfilled. In all cases, $\vartheta_{in} = 25^\circ\text{C}$ was specified at the upstream periodic boundary as target value for the bulk temperature of the flow. A further geometrical reduction was achieved by making use of the symmetry of the flow channels in z -direction (cf. Fig. 4).

At the vertical boundaries, at $x = 0$ and $x = 0.5s_T$, as well as at the horizontal boundaries representing the mid-planes of IC and OC, respectively, symmetry boundary conditions were set. They mainly comprise zero-gradient boundary conditions for the velocity components and temperature, as well as the Dirichlet boundary condition $\vec{u} \cdot \vec{n} = 0$ for the normal velocity component. At the curved boundaries, which represent the surfaces of the pillow plate, the wall boundary conditions were applied. They include zero-value Dirichlet boundary conditions for all velocity components (no-slip) and the specification of a constant wall temperature of $\vartheta_w = 30^\circ\text{C}$. All boundary conditions are summarised in Fig. 4.

5.4. Boundary conditions for conjugate heat transfer simulations

For the CHT simulations, the computational domains of IC and OC were extended in primary flow direction (y -direction, cf. Fig. 5). Each channel was composed of 7 periodic simulation elements (cf. Fig. 4). This increases the length of the computational domains to $L_{SD} = 14 \cdot s_L = 504$ mm. In contrast to the uncoupled simulations for IC and OC flow, no periodic boundary conditions were used in this case, since the scaling of the temperatures from the outflow to the inflow boundaries was found to be incorrect due to the wall temperatures that were no longer constant. Instead, velocity inlets were used at the inflow boundaries and a countercurrent flow configuration was realised by an opposite arrangement of the inlets (cf. Fig. 5). The velocity inlets were defined using the corresponding fully developed fields for velocity and turbulence quantities, which were obtained from the previously performed uncoupled CFD simulations for IC and OC flow. The temperature at the inlets was defined by a constant value, with inlet temperatures of $\vartheta_{in,IC} = 25^\circ\text{C}$ for IC and $\vartheta_{in,OC} = 50^\circ\text{C}$ for OC flow, resulting in heat transfer from OC to IC flow. Since the flow profiles at the inlet boundaries are defined as hydrodynamically fully developed and due to turbulent mixing processes, it can be assumed that the thermal entrance length is very short (confirmation is shown in Section 6). For all other quantities, a zero-gradient condition applies to the inlets.

At the outlet boundaries of IC and OC, a pressure outlet boundary condition was used, with temperature of the re-entering backflow being set equal to the bulk temperature of the exiting flow. Symmetry boundary conditions were applied to all lateral boundaries ($x = 0$, $x = 0.5s_T$). In addition, to keep the simulation domain as small as possible, symmetry boundary conditions were also used for the mid-planes of the channels and the welding spots. Furthermore, symmetry boundary conditions were also defined for the vertical boundaries of the metal sheet at the positions $y = 0$ and $y = 14 \cdot s_L$. The thermal coupling between the fluid

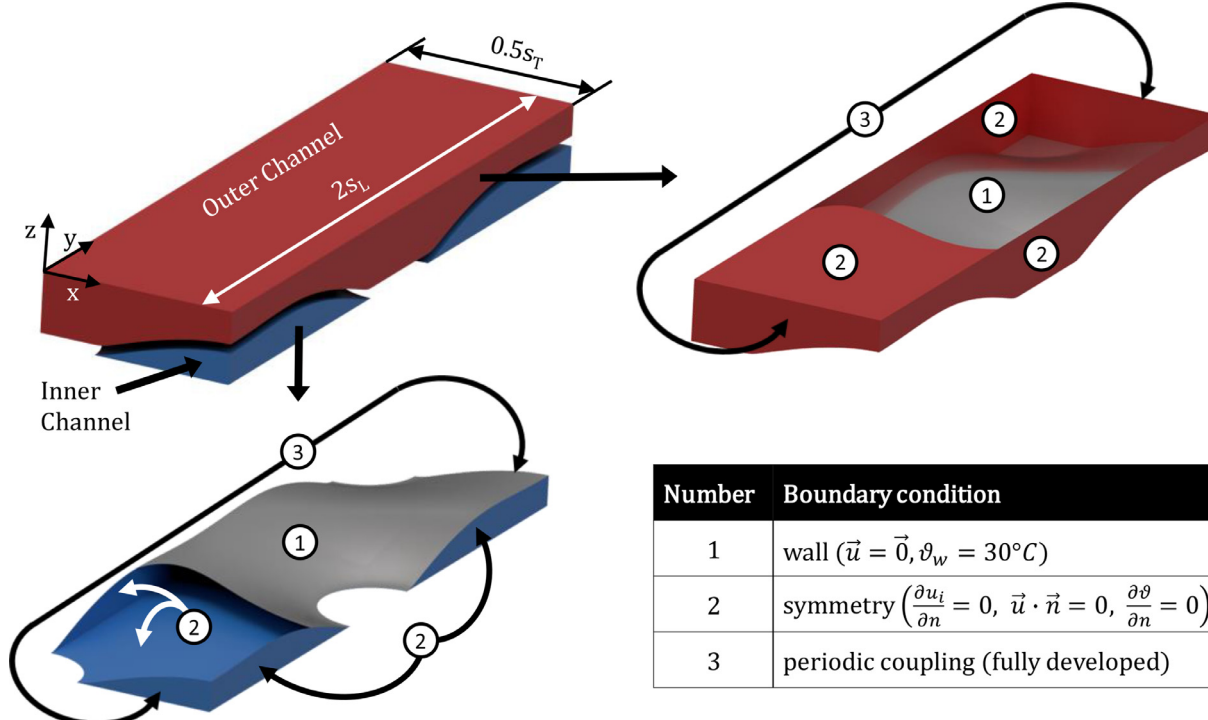


Fig. 4. Periodic computational domains of IC and OC used for the uncoupled simulations, together with the applied boundary conditions; top surfaces of the simulation domains for OC (top right) and IC (bottom left) flow are cut, allowing a view into the volume.

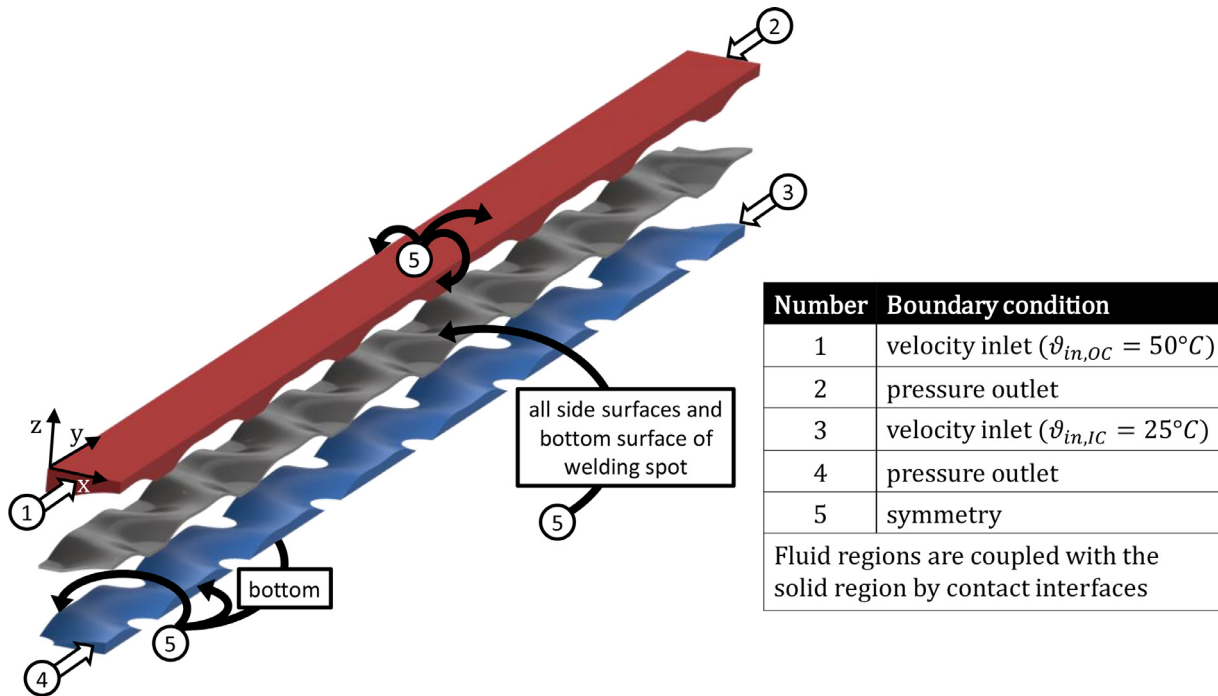


Fig. 5. Computational domains of IC, plate and OC used for the CHT simulations, together with the applied boundary conditions.

regions and the solid region (metal sheet) was realised by means of contact interfaces.

6. Validation

For IC flow, data from [9] obtained with correlations for Darcy friction factor and Nusselt number were taken as reference for the validation of the uncoupled CFD simulations carried out in this work.

As can be seen in Fig. 6a, the pressure drop obtained by the simulation are about 5% lower than the correlation data, while the heat transfer is overestimated by about 10% (Fig. 6b). Considering

that the correlations taken from [9] have an accuracy of $\pm 6\%$ for Darcy friction factor and $\pm 15\%$ for Nusselt number, it can be concluded that the simulation results are within the accuracy of the correlations.

For OC flow, both experimental and numerical results of Piper et al. [11] were used as a validation basis for the arising pressure drop, which was obtained for exactly the same pillow plate geometry as investigated in this work. However, there is no experimental data available for heat transfer, and thus, a comparison with simulation results taken from [11] was performed. As can be seen in Fig. 7a, the pressure drop is overestimated by 10% as compared to experimental data and by 8% with respect to the simulation results

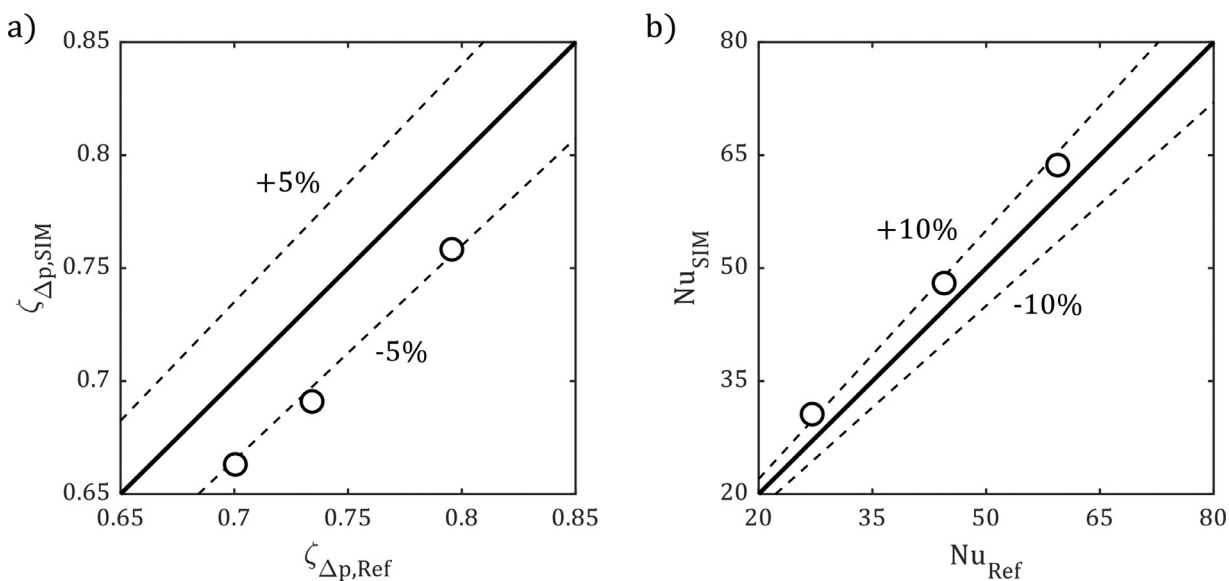


Fig. 6. Comparison of Darcy friction factor (a) and Nusselt number (b) for IC flow obtained from simulations carried out in this work with data from correlations of Piper et al. [9].

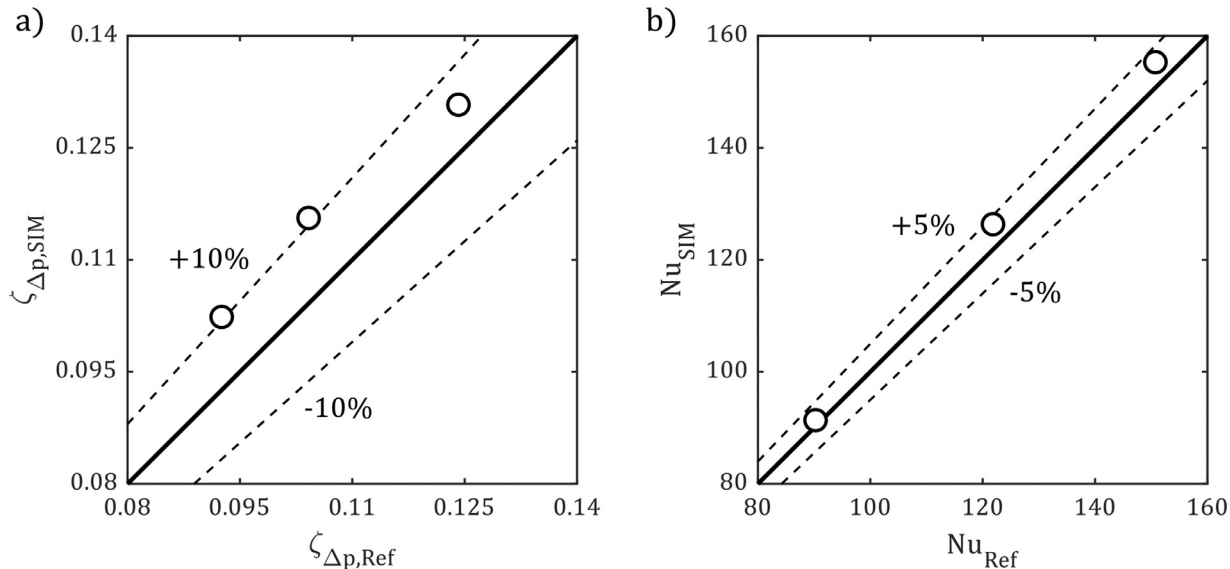


Fig. 7. Comparison of the simulation results for OC flow Darcy friction factor (a) and Nusselt number (b) with experimental and numerical results of Piper et al. [11].

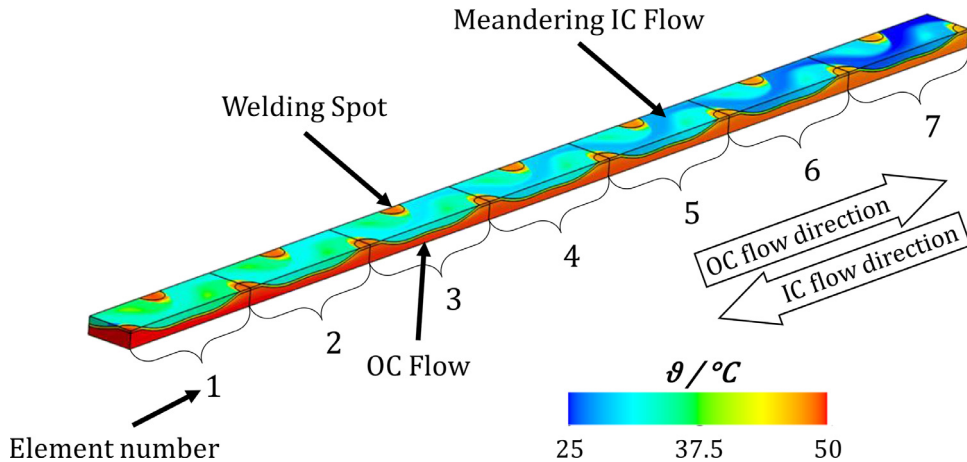


Fig. 8. Exemplary visualisation of the temperature distribution resulting from the CHT simulations (simulation case C3, $\delta_p = 1$ mm, steel).

of Piper et al. [11]. For heat transfer, the deviation is less than 4% (cf. Fig. 7b). Thus, we have reasons to believe that the simulations carried out in this study capture the transport phenomena in IC and OC of a PPHX with adequate accuracy.

In case of the CHT simulations, the IC and OC flows are defined hydrodynamically fully developed at the inlet boundaries, but temperature is specified to be constant over the inlet cross sections. Therefore, it was examined whether IC and OC flow can thermally fully develop within the length of the selected simulation domain. As an example, the temperature field resulting from the CHT simulations for Case C3 (cf. Table 1) is shown for the entire simulation domain in Fig. 8.

Clearly visible is the meandering primary flow of IC as well as the recirculation zones formed behind the welding spots, which have a flame-like shape and can be identified by increased fluid temperature compared to the primary flow. As described in Section 5.4, the entire simulation domain can be subdivided into 7 periodic elements, so that the mean heat transfer coefficients for IC and OC flow may be evaluated elementwise (cf. Fig. 8). The resulting curves, shown in Fig. 9, prove that the thermal development of IC as well as OC flow is already completed in the second periodic element after flow entry, since the resulting heat transfer coefficients become constant. For reasons of accuracy, however, the size of the simulation domain was not reduced, while the evaluation of

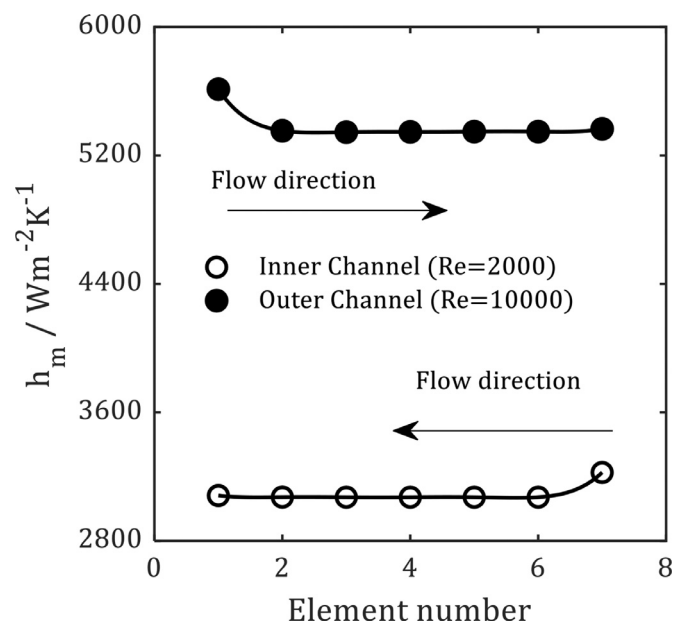


Fig. 9. Element-wise averaged heat transfer coefficients of IC and OC flow (simulation case C3, $\delta_p = 1$ mm, steel).

the CHT simulations was limited only to the central periodic element (element number 4, cf. Fig. 8).

7. Results & discussion

In almost all cases (C2-C5, $\delta_p \in \{1 \text{ mm}, 2 \text{ mm}\}$), the CHT simulations revealed that the total thermal resistance of the examined PPHX ($r_{th,tot}$) is dominated by $r_{th,IC}$ (cf. Fig. 10), whereas the thermal resistance of the metal sheet ($r_{th,P}$) represents the smallest portion of $r_{th,tot}$. However, in cases C3-C5 with $Re_{OC} = 10000$, $r_{th,P}$ can reach values comparable to $r_{th,OC}$, if the pillow plates are made of steel with $\delta_p = 2 \text{ mm}$. Furthermore, it can be seen that in case of steel, $r_{th,P}$ is approximately proportional to δ_p , whereas in case of aluminium, $r_{th,P}$ is hardly dependent on the thickness of the metal sheet. This issue is examined in more detail below. It can be stated at this point, that if pillow plates are made of aluminium and not stainless steel as usual, a reduction of $r_{th,tot}$ by 10-25% can be achieved depending on the operating condition. This allows PPHX to be more compact and lighter, and reduces operating costs, as shorter flow lengths reduce the pressure drop and thus the required pumping power.

For Case C3, Fig. 11 shows exemplarily the resulting heat flux distribution on the pillow plate surface adjacent to OC flow, with values being normalised by the appearing maximum value. Here, Fig. 11a represents the result of the uncoupled simulation with constant wall temperature boundary condition, while Fig. 11b and c show results of the CHT simulations ($\delta_p = 1 \text{ mm}$, steel/aluminium sheet).

In Fig. 11a the sickle-shaped blue regions clearly mark the locations where separation of OC flow from the pillow plate surface occurs, resulting in poor heat transfer due to forming recirculation zones. The red regions on the welding spot surfaces, on the other hand, indicate the locations where the flow reattaches and causes a maximum in terms of heat flux owing to the prevailing high temperature and velocity gradients. After passing the welding spots, the flow is strongly reaccelerated as a result of the pillow plate curvature and the associated reduction of the channel cross-

section, creating further heat flux maxima induced by the thinning of the boundary layer. When using a pillow plate made out of stainless steel, the welding spot surfaces are thermally nearly inactive, because of the low thermal conductivity of the sheet material (cf. Fig. 11b). On the other hand, Fig. 11c shows that with aluminium as sheet material, the welding spot surfaces have a significantly higher thermal activity. Furthermore, the higher thermal conductivity of aluminium causes the resulting heat flux distribution to shift towards the results of the constant wall temperature simulation case (Fig. 11a), which in principle corresponds to the scenario of an infinitely high thermal conductivity of the sheet and thus $\eta_{SP} = 1$. In contrast, Fig. 11b reveals that the inefficient heat transfer in the recirculation zones of IC flow can also have a negative effect on the OC heat transfer, when the pillow plate is made out of steel. The reason for this effect is the weak in-plane heat transfer in the sheet owing to the low thermal conductivity of steel.

This becomes even more clear from Fig. 12, where the resulting temperature fields in the sheet are shown. It can be seen that the isotherms in the aluminium sheet are oriented much more orthogonally to the sheet surface than in the steel sheet and bend less pronouncedly in the vicinity of the welding spot edges. Thus, in the steel sheet, heat transported normally to the sheet plane is dominating, while in the aluminium sheet, in-plane heat transport is not negligible. This can be attributed to the significantly better thermal conductivity of aluminium, resulting in more heat being absorbed by the welding spot surfaces and transported in the radial direction of the welding spots. It can also be seen that in the steel sheet, the temperature gradient vanishes almost exactly in the centre of a welding spot (cf. Fig. 12). This shows a very good agreement with the modelling assumption that a welding spot is composed of several triangular fins (cf. Fig. 2). According to this approach, the tips of the fins meet at the centreline (normal to the sheet surface) of the welding spots, so that in-plane heat transport vanishes due to the line-contact of the fin tips resulting in hot spots at the centre of the welding spots. For the aluminium

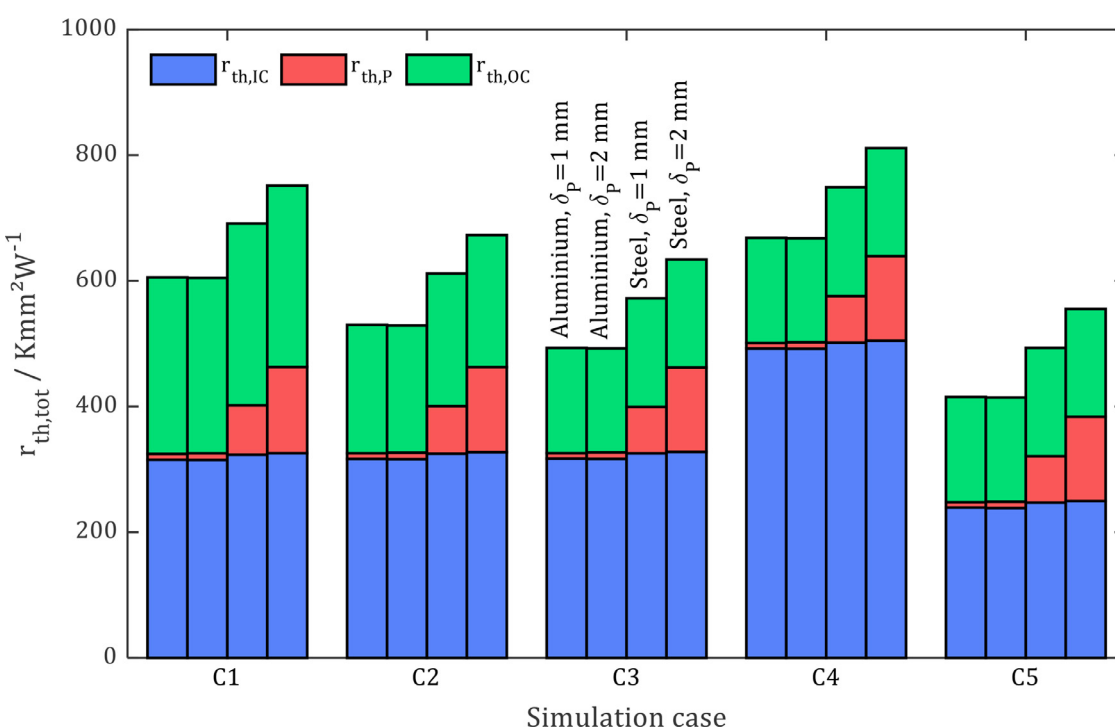


Fig. 10. Total specific thermal resistance with portions of the partial resistances $r_{th,IC}$, $r_{th,P}$, $r_{th,OC}$.

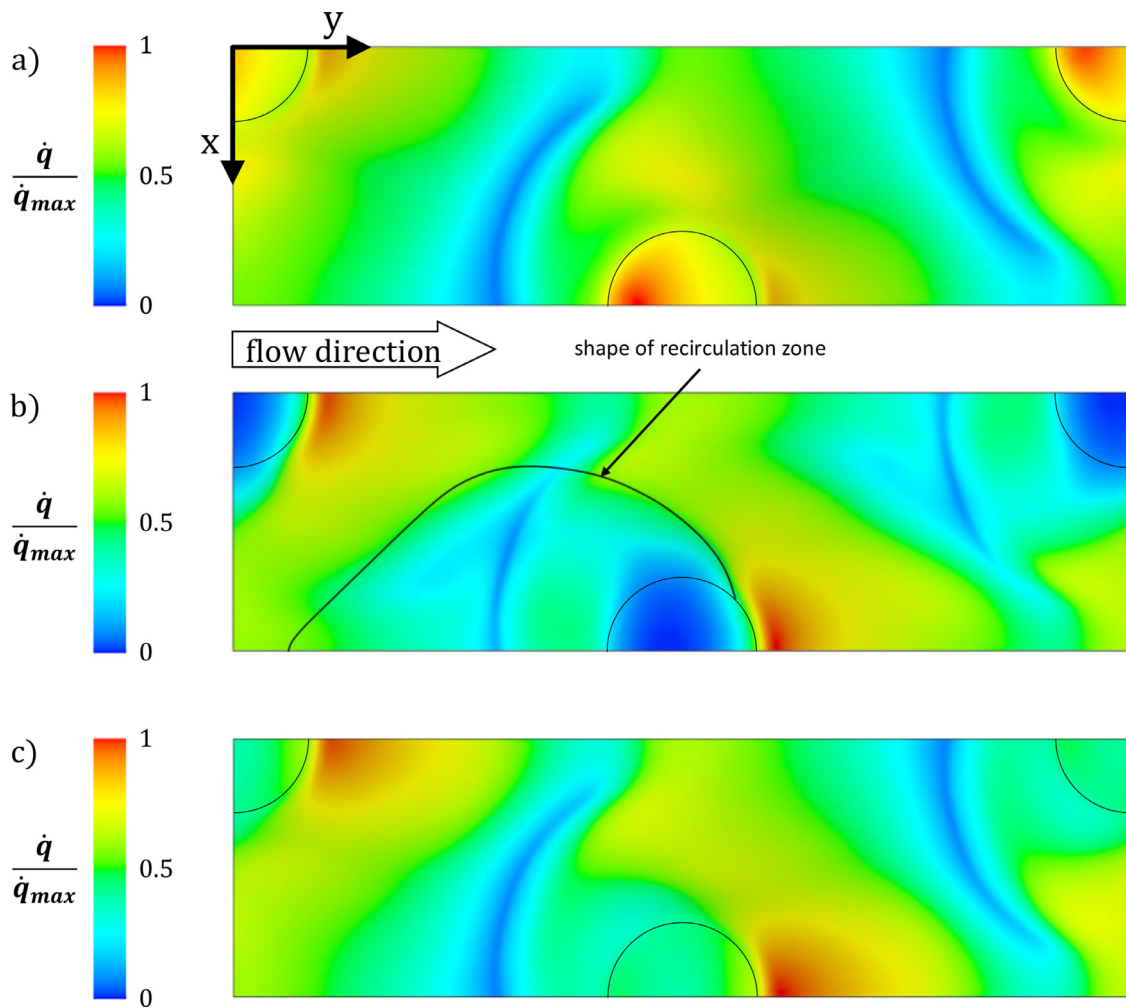


Fig. 11. Distributions of normalised heat flux on the pillow plate surface adjacent to OC flow for the uncoupled simulation case (a), the CHT simulation case C3 ($\delta_p = 1$ mm, steel) (b) and the CHT simulation case C3 ($\delta_p = 1$ mm, aluminium)(c). In (b) additionally the shape of the recirculation zones of IC flow is shown.

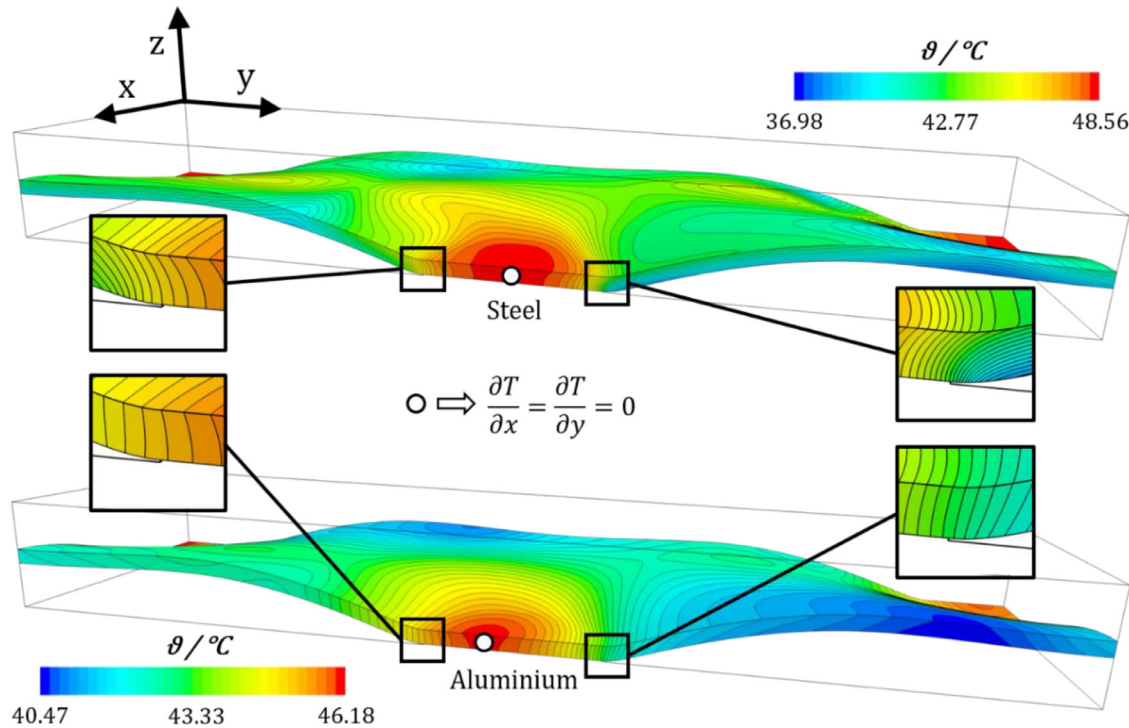


Fig. 12. Temperature distribution with isolines in the plate for CHT simulation of case C3 ($\delta_p = 1$ mm).

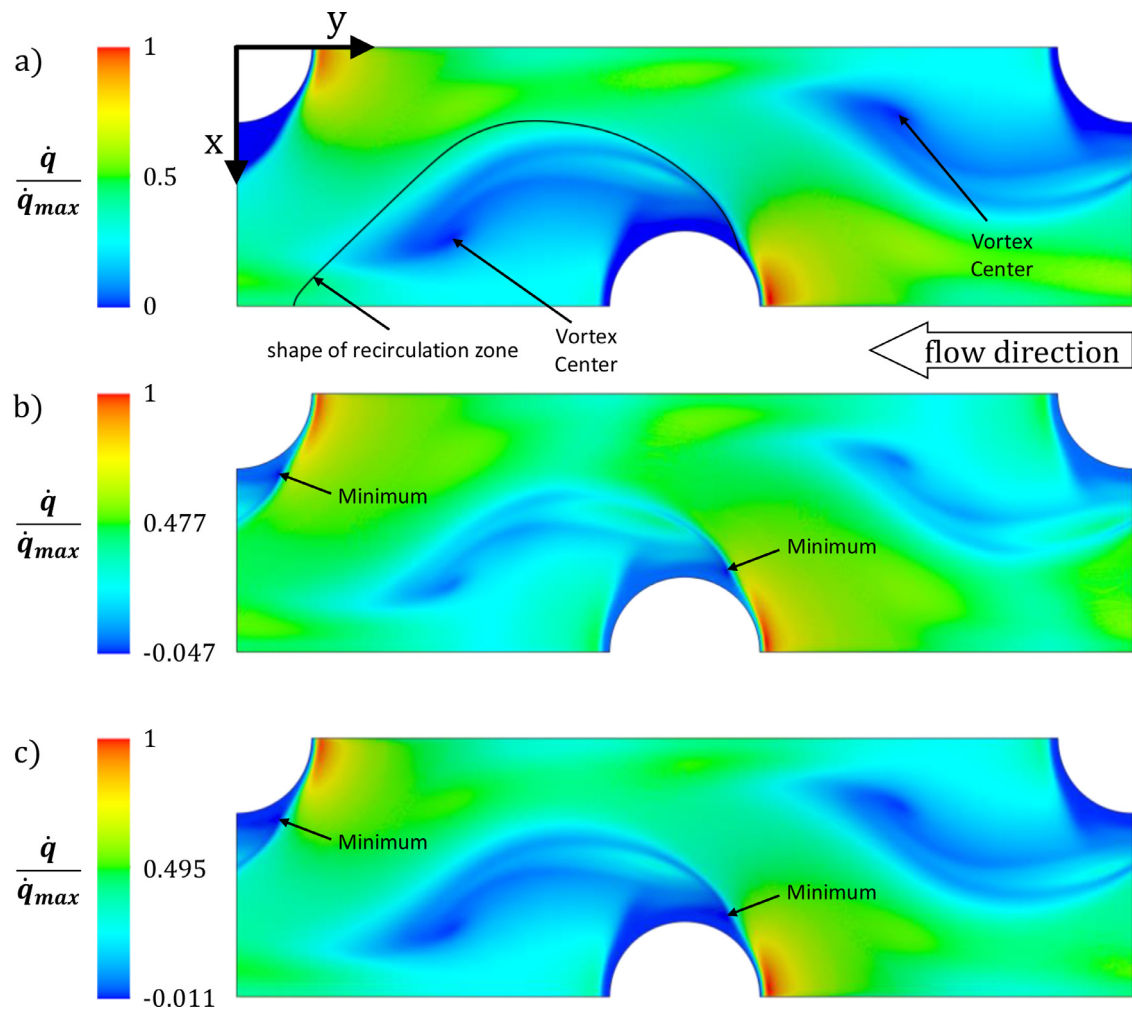


Fig. 13. Distributions of normalised heat flux on the pillow plate surface adjacent to IC flow for the uncoupled simulation case (a), the CHT simulation case C3 ($\delta_p = 1$ mm, steel) (b) and the CHT simulation case C3 ($\delta_p = 1$ mm, aluminium)(c). In (a), the shape of the recirculation zones of IC flow is additionally shown.

sheet, this point is slightly shifted from the welding spot centre into negative y -direction.

Fig. 13 is the counterpart to Fig. 11 and shows, exemplarily for case C3, the heat flux distribution on the sheet surface adjacent to IC flow. Again, the values were normalised to the maximum occurring flux value. It is clearly visible that the heat transport is most intensive in the area covered by the meandering primary flow (cf. Fig. 8). However, in the flame-shaped recirculation zones that form downstream of the welding spots, heat transfer is significantly reduced. Especially pronounced is this heat transfer reduction in the direct vicinity of the welding spots as well as at the vortex centres of the recirculation zones, where local minima of the normalised heat flux appear (cf. Fig. 13a). The most intensive heat transfer, on the other hand, takes place at the stagnation points in the frontal area of the welding spots, since the highest velocity and thus also temperature gradients are found around these points. Basically, the heat flux distributions resulting from the CHT simulations (Fig. 13b and c) show a clear similarity with the results of the uncoupled simulation of the IC flow (Fig. 13a) performed with constant wall temperature boundary condition. It can therefore be assumed that for IC flow, the sheet material and sheet thickness have lower influence on the heat transfer than for OC flow. However, it is noteworthy that in case of the CHT simulations, the heat transport partially reverses, which can be seen from the occurring negative values of the normalised heat flux. This is due to the fact that recirculating fluid heats up considerably in the immediate

vicinity of the welding spots, while at the edge of the recirculation zones (shear layer between backflow and primary flow), wall temperature drops quickly due to the more intensive heat transfer in this region. For this reason, the fluid temperature can locally exceed the wall temperature, so that the direction of heat transfer reverses.

The parity plots in Fig. 14 show a comparison of the thermal resistances of OC flow resulting from the CHT simulations with the theoretically calculated thermal resistances according to Eq. (19). All presented values correspond to $Re_{IC} = 2000$, since the simulations showed that the influence of Re_{IC} on $r_{th,OC}$ is negligible. Three different cases were considered, in which the welding spot surfaces were either thermally fully active ($\eta_{SP} = 1$), fully inactive ($\eta_{SP} = 0$) or have a fin efficiency according to Eq. (17), with values plotted in dependence of Re_{OC} in Fig. 15. It can be seen that for pillow plates made out of steel (Fig. 14a and b), the assumption of thermally fully inactive welding spots (maximum deviation for $\delta_p = 1$ mm is about +3.7%, or about +3.9% for $\delta_p = 2$ mm) is more justified than thermally fully active welding spots (maximum deviation for $\delta_p = 1$ mm is about -5.9%, or about -5.2% for $\delta_p = 2$ mm). This could be expected already from the analysis of Fig. 11; the latter also shows for aluminium the opposite behaviour. Thus, the thermal resistances calculated under the assumption of thermally fully active welding spots meet the simulation results with high accuracy (maximum deviation for $\delta_p = 1$ mm is about -2.6%, or about -1.5% for $\delta_p = 2$ mm), whereas $r_{th,OC}$ is clearly overestimated in case

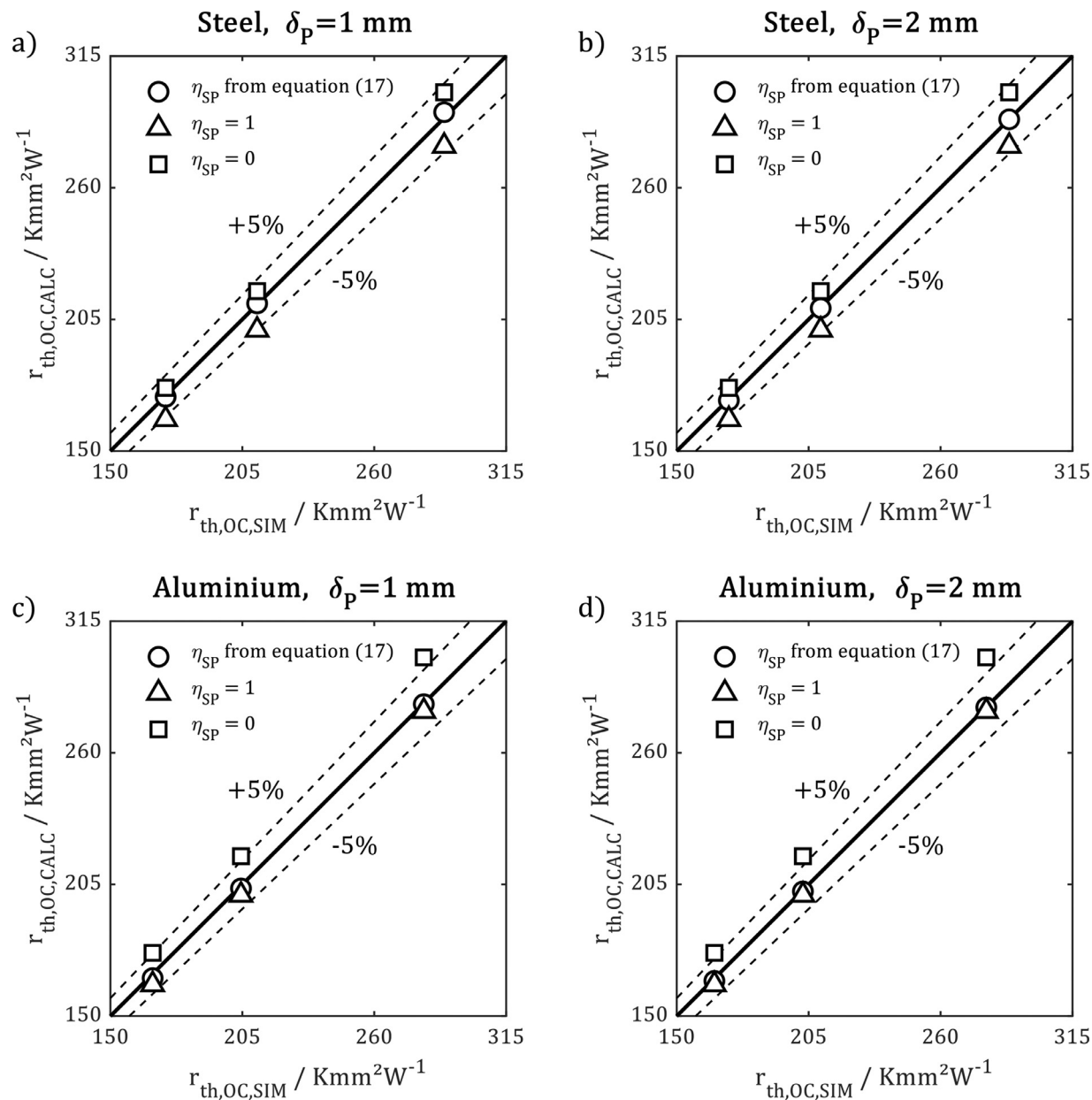


Fig. 14. Comparison of the thermal resistance of OC flow calculated according to Eq. (19) with results of the CHT simulations. The shown values always correspond to $Re_{OC} = 2000$.

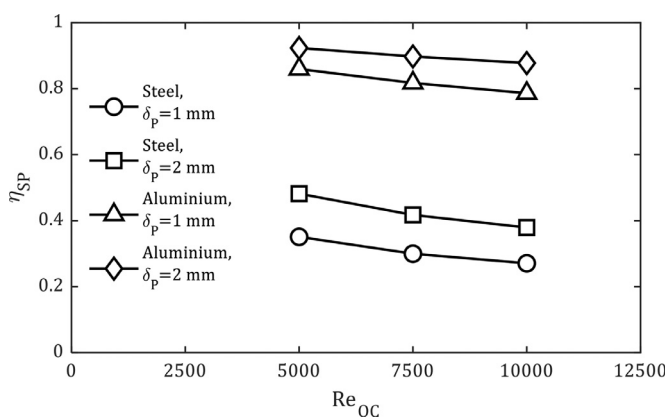


Fig. 15. Fin efficiency of the welding spots in dependence on Re_{OC} .

of $\eta_{SP} = 0$ (maximum deviation for $\delta_p = 1$ mm is about +6.8%, or about +7.4% for $\delta_p = 2$ mm).

However, in all cases, the thermal resistances calculated with η_{SP} according to Eq. (17) show the best agreement with the simulation results. This gives a maximum deviation of +0.8% for steel with $\delta_p = 1$ mm and -0.4% for $\delta_p = 2$ mm. The deviations are similarly low for aluminium as sheet material. For instance, the maximum deviation in this case is -1% for $\delta_p = 1$ mm and for $\delta_p = 2$ mm, the maximum deviation is -0.6%.

In Fig. 16a and b, it can be seen that the thermal resistance of the metal sheet is always underestimated when calculated according to Eq. (22). Furthermore, it can be seen that the deviations increase with decreasing sheet thickness. For steel, a maximum deviation of -15.1% was observed for $\delta_p = 1$ mm, while for $\delta_p = 2$ mm it is only -2.9%. However, the thermal conductivity of the sheet material influences the thermal resistance much more significantly than δ_p , so that the deviations of the calculated thermal resistances from the simulation results are much higher for

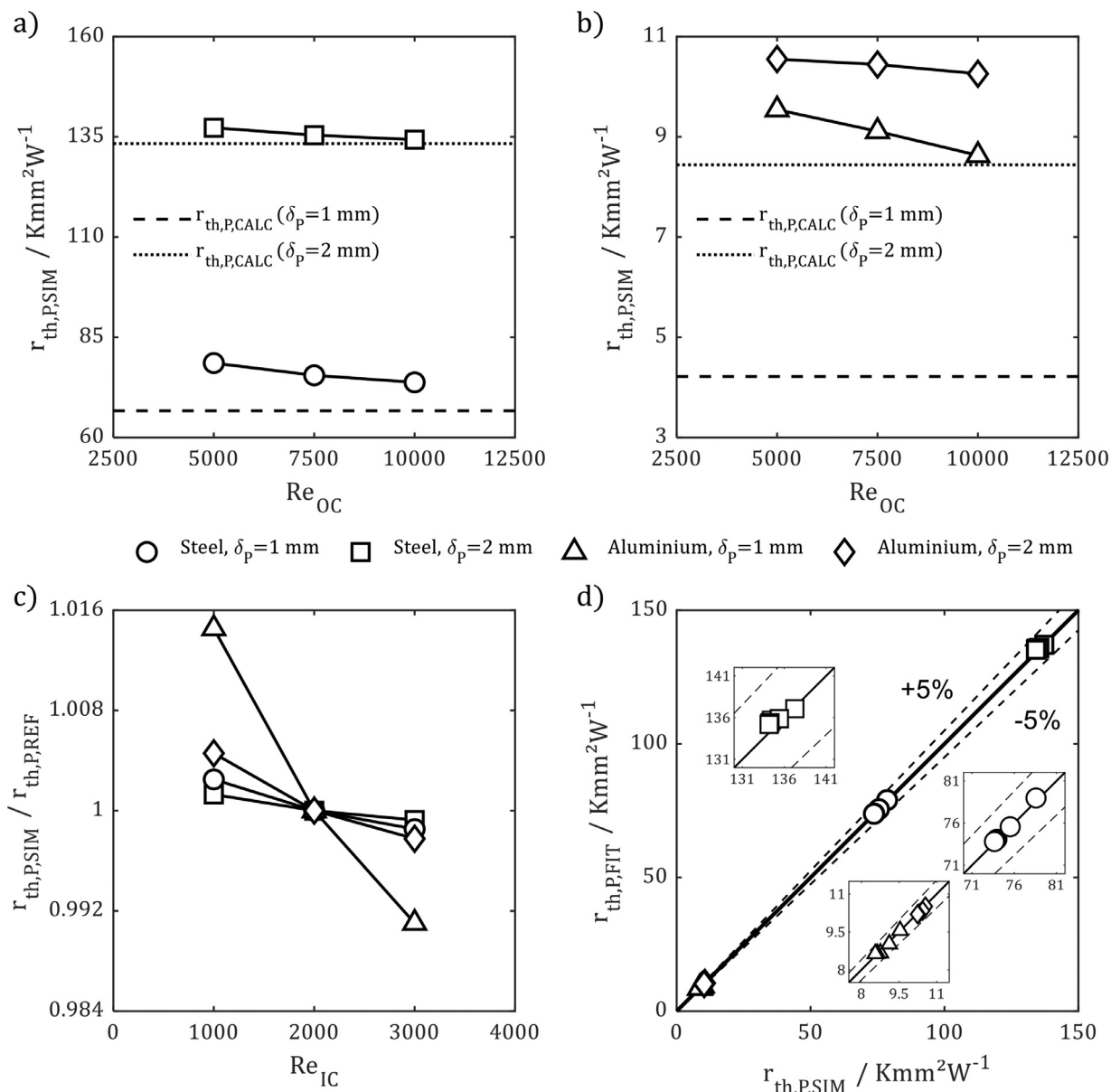


Fig. 16. Thermal resistance of the plate in case of steel (a) and aluminium (b) for $Re_{IC} = 2000$ in dependence of Re_{OC} ; Thermal resistance of the plate for $Re_{OC} = 10000$ normalised by the value corresponding to $Re_{IC} = 2000$ (c); Comparison of the thermal resistance of the plate calculated with the aid of the fit function (Eq. (28)) with simulation results (d)

aluminium than for steel (Fig. 16b). For an aluminium sheet with $\delta_p = 2 \text{ mm}$, deviations reach up to -20%; with $\delta_p = 1 \text{ mm}$, they can be as high as -55.8%. These deviations can be explained by the fact that heat is not transported purely orthogonally to the sheet surface, as assumed in the calculations.

Looking at the welding spot region, heat transferred by OC flow to the outer surfaces of a welding spot must first be conducted in the plane of the sheet in radial direction up to the edge of the welding spot, as illustrated in Fig. 17. This in-plane heat transport also continues beyond the edge of the welding spot, with heat also being partially transported to IC flow. As the thermal conductivity of the sheet material increases, η_{SP} increases, so that significantly more heat is absorbed by the welding spot surfaces. The more heat is absorbed by the welding spot surfaces, the more pronounced is the in-plane heat conduction in the vicinity of the welding spots. This explains why the isotherms at the edge of a welding spot bend more significantly in a steel sheet than in an aluminium

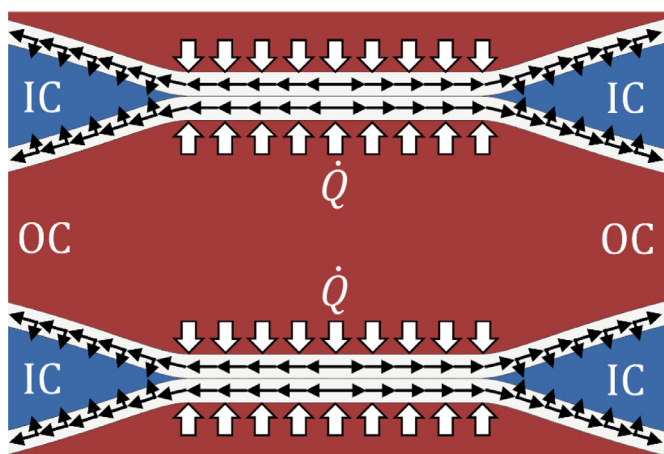


Fig. 17. Illustration of the flow path of heat, which is absorbed by the welding spot surfaces.

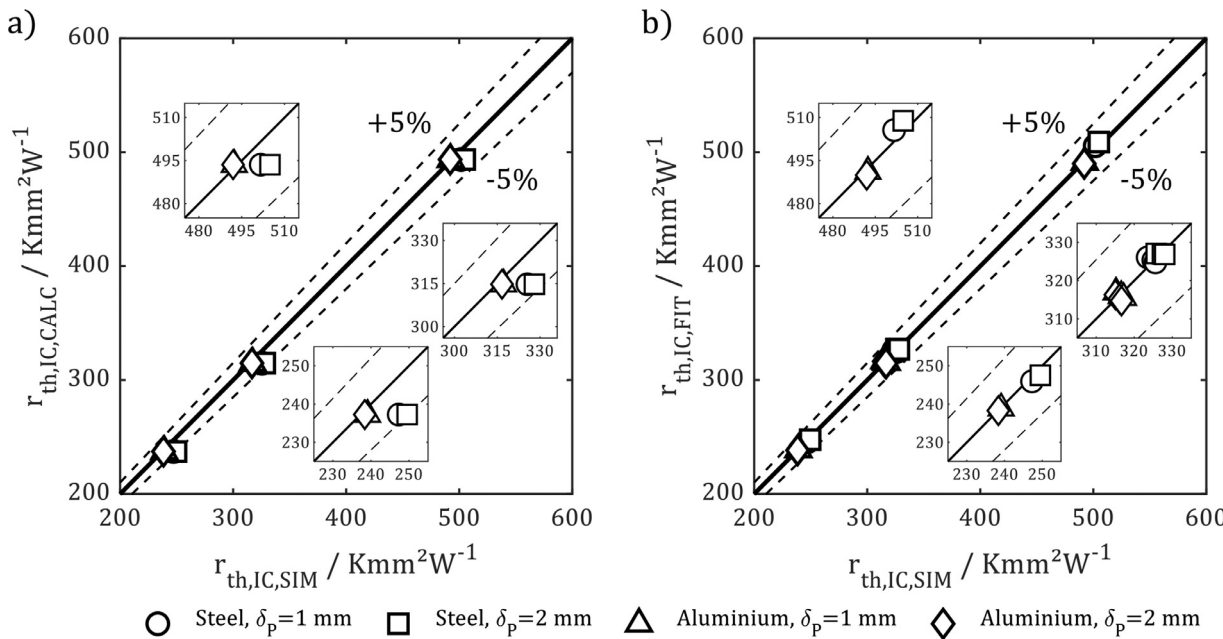


Fig. 18. Comparison of the thermal resistance of IC flow calculated according to Eq. (26) with results of the CHT simulations for $Re_{OC} = 10000$ (a); Comparison of the thermal resistance of IC flow calculated with the aid of the fit function (29) with total CHT simulation results (b).

sheet (cf. Fig. 12). This effect also results in increasing contribution of the additional thermal resistance due to the in-plane heat conduction to the total thermal resistance of the metal sheet. This in turn explains the significantly larger deviations of the calculated thermal resistances for aluminium compared to steel. Furthermore, increasing deviations with decreasing plate thickness can also be attributed to the in-plane heat conduction, since with decreasing plate thickness, the cross-section available for in-plane heat conduction reduces. As a result, the additional thermal resistance for in-plane heat transport increases and leads to a higher total resistance of the sheet. By comparing Fig. 16c with 16a and b, it becomes evident that $r_{th,P}$ is much less dependent on Re_{IC} than on Re_{OC} . Consequently, this means that the thermal resistance of the metal sheet depends more strongly on the heat transfer coefficient of the OC flow than on the heat transfer coefficient of the IC flow.

To derive a fit function for the thermal resistance of the metal sheet, the thermal conductivity of the sheet material resp. the fin efficiency of the welding spots as well as the sheet thickness were identified as main influencing factors. Furthermore, the heat transfer coefficients of the OC and IC flow were also included as less significant influencing parameters. Using the fit function given by the following equation (with $\delta_{P,Ref} = 1$ mm)

$$f_{FIT,P} = \frac{1}{\left[1.11 - 0.79 \cdot \left(\frac{\delta_p}{\delta_{P,Ref}} \right)^{-1.2} \cdot \eta_{SP} \right] \cdot \left(\frac{\hat{h}_{m,OC}}{\hat{h}_{m,IC}} \right)^{0.01}}, \quad (28)$$

the thermal resistance of the metal sheet can be calculated according to Eq. (23) with an accuracy of $\pm 2\%$ (cf. Fig. 16d).

The thermal resistance of IC flow can be calculated very precisely using Eq. (26) for pillow plates made from aluminium. The maximum deviation for $\delta_p = 1$ mm is approx. 0.8%, or approximately -0.6% for $\delta_p = 2$ mm (cf. Fig. 18a). In case of steel, however, there is a deviation of up to 4.9%, while the calculated values always underestimate the simulation results. To reduce this deviation, a fit function (Eq. (29)) was derived, which is based on the same parameters as $f_{FIT,P}$. This allows the thermal resistance of the IC flow to be calculated with an accuracy of $\pm 0.8\%$ by using

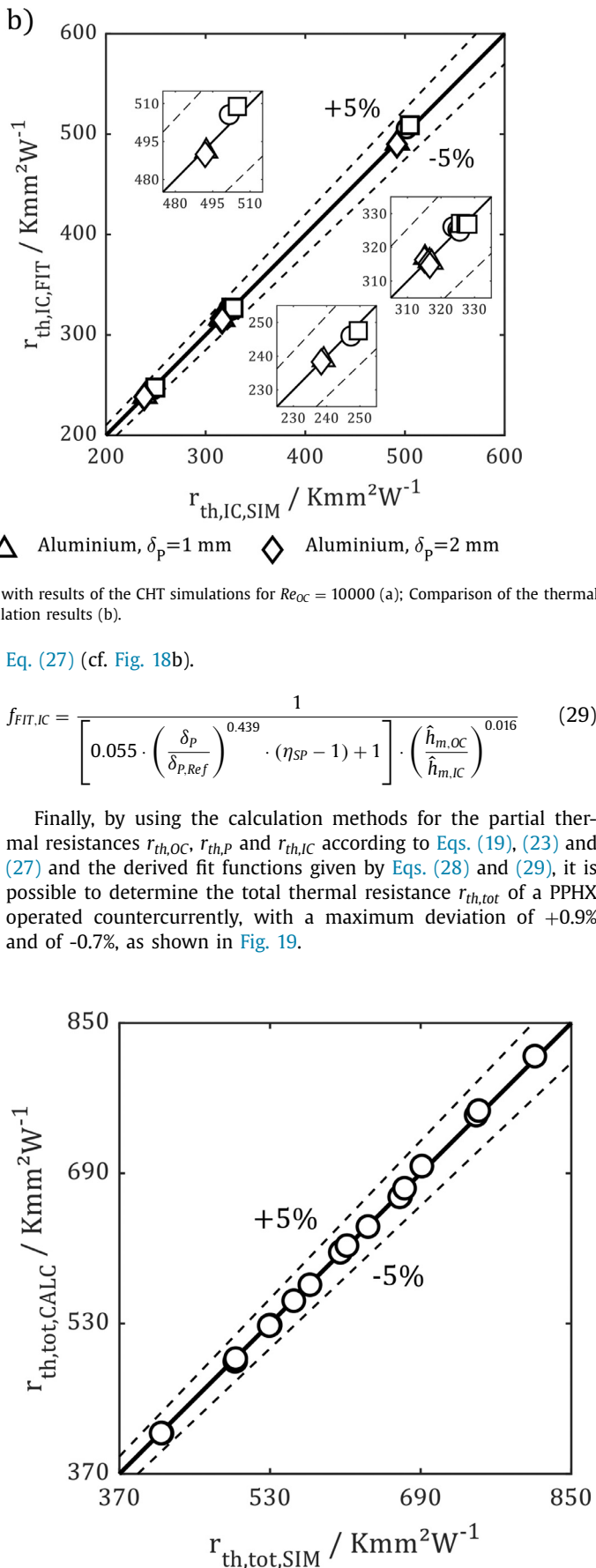


Fig. 19. Comparison of the calculated total thermal resistance of the PPHX with simulation results.

8. Conclusions

For the first time, conjugate heat transfer simulations were performed for a pillow-plate heat exchanger (PPHX), resulting in a realistic reproduction of the coupled heat transport between inner channel (IC) flow, metal sheet and outer channel (OC) flow. This is a substantial progress against uncoupled simulations for either IC or OC flow published up to now.

Due to its significantly higher thermal conductivity, aluminium represents a promising alternative to stainless steel for the production of pillow plates. For this reason, both stainless steel and aluminium were considered as sheet materials in the simulation studies. The simulations showed that using aluminium can reduce the total thermal resistance of a PPHX by 10–25%. This in turn results in a lighter and more compact design of PPHX as well as in reduced operating costs, since pressure drop and thus the required pumping power can be decreased due to reduction of the overall heat exchanger length.

Furthermore, a detailed analysis of the partial thermal resistances of IC flow, metal sheet and OC flow was carried out. For OC flow, it was shown that the welding spots, which, compared to IC channel, increase the active heat transfer surface, act in an analogous way as fins and hence can be treated similarly. Therefore, approaches for the calculation of the fin efficiency of the welding spots and for the calculation of the thermal resistance of OC flow were suggested. Using these approaches, the thermal resistance of the OC flow can be determined with an accuracy of approximately $\pm 1\%$.

Regarding the thermal resistance of the sheet, it was shown that with increasing thermal conductivity of the material, an additional thermal resistance arises due to in-plane heat conduction, which is not negligible. As a result, assuming one-dimensional heat conduction leads to an underestimation of the sheet thermal resistance by more than 50% in case of aluminium. Hence, a fit function was obtained to take into account the three-dimensional nature of the heat transport prevailing in the metal sheet, which allows the calculation of the thermal resistance of the metal sheet with an accuracy of $\pm 2\%$.

For IC flow, comprehensive Nusselt correlations have already been published by Piper et al. [9], yielding predictable heat transfer coefficients and thus thermal resistances of IC flow. However, these correlations are based on simplified CFD simulations focusing on a separated section of an IC channel. Moreover, a constant wall temperature boundary condition was specified, which only rarely corresponds to reality. For this reason, a fit function was derived in this study to correct the thermal resistances based on the methods by Piper et al. [9] in order to take into account the influence of conjugate heat transfer in a PPHX. Using this fit function, the thermal resistance of the IC flow can be determined with a deviation of less than 1% for the PPHX configuration investigated in this paper.

Declaration of Competing Interest

The authors declare that they have no known competing financial interests or personal relationships that could have appeared to influence the work reported in this paper.

CRediT authorship contribution statement

A. Zibart: Conceptualization, Methodology, Software, Validation, Writing - original draft. **E.Y. Kenig:** Methodology, Writing - review & editing, Supervision, Resources.

Acknowledgments

The authors gratefully acknowledge the funding of this project by computing time provided by the Paderborn Center for Parallel Computing (PC²).

References

- [1] J. Mitrovic, R. Peterson, Vapor condensation heat transfer in a thermoplate heat exchanger, *Chem. Eng. Technol.* 30 (7) (2007) 907–919.
- [2] J. Mitrovic, B. Maletić, Numerical simulation of fluid flow and heat transfer in thermoplates, *Chem. Eng. Technol.* 34 (9) (2011) 1439–1448.
- [3] M. Piper, A. Olenberg, J.M. Tran, R. Goedecke, S. Scholl, E.Y. Kenig, Bestimmung charakteristischer Geometrieparameter von Thermoblech-Wärmeübertragen, *Chem. Ing. Tech.* 86 (4) (2014) 1214–1222.
- [4] M. Piper, A. Olenberg, J.M. Tran, E.Y. Kenig, Determination of the geometric design parameters of pillow-plate heat exchangers, *Appl. Therm. Eng.* 91 (2015) 1168–1175.
- [5] M. Piper, A. Zibart, J.M. Tran, E.Y. Kenig, Numerical investigation of turbulent forced convection heat transfer in pillow plates, *Int. J. Heat Mass Transfer* 94 (2016) 516–527.
- [6] T.-H. Shih, W.W. Liou, A. Shabbir, Z. Yang, J. Zhu, A new $k-\varepsilon$ eddy viscosity model for high reynolds number turbulent flows, *Comput. Fluids* 24 (3) (1995) 227–238.
- [7] J.M. Tran, M. Piper, E.Y. Kenig, Experimentelle Untersuchung des konvektiven Wärmeübergangs und Druckverlustes in einphasig durchströmten Thermoblechen, *Chem. Ing. Tech.* 87 (3) (2015) 226–234.
- [8] J.M. Tran, S. Sommerfeld, M. Piper, E.Y. Kenig, Investigation of pillow-plate condensers for the application in distillation columns, *Chem. Eng. Res. Des.* 99 (2015) 67–74.
- [9] M. Piper, A. Zibart, E.Y. Kenig, New design equations for turbulent forced convection heat transfer and pressure loss in pillow-plate channels, *Int. J. Therm. Sci.* 120 (2017) 459–468.
- [10] M. Piper, J.M. Tran, E.Y. Kenig, CFD-Untersuchung der Fluidodynamik und des Wärmeübergangs bei einphasiger Strömung im welligen Spalt zwischen Thermoblechen, *Chem. Ing. Tech.* 87 (3) (2015) 216–225.
- [11] M. Piper, J.M. Tran, E.Y. Kenig, A CFD study of the thermo-hydraulic characteristics of pillow-plate heat exchangers, in: *Proceedings of the ASME 2016 Heat Transfer Summer Conference*, 2016 HT2016-7176:1–7.
- [12] F. Billard, D. Laurence, A robust $k-\varepsilon-\bar{v}^2/k$ elliptic blending turbulence model applied to near-wall, separated and buoyant flows, *Int. J. Heat Fluid Flow* 33 (2012) 45–58.
- [13] H.D. Baehr, K. Stephan, *Heat and Mass Transfer*, Springer-Verlag, Berlin Heidelberg, 2011.
- [14] S. Lardeau, F. Billard, Development of an elliptic-blending lag model for industrial applications, in: *54th AIAA Aerospace Sciences Meeting*, 2016, p. 1600.
- [15] M. Wolfshtein, The velocity and temperature distribution in one-dimensional flow with turbulence augmentation and pressure gradient, *Int. J. Heat Mass Transfer* 12 (3) (1969) 301–318.